

# Muography

Hiroyuki K. M. Tanaka<sup>1,2</sup>✉, Cristiano Bozza<sup>1,3</sup>, Alan Bross<sup>1,4</sup>, Elena Cantoni<sup>1,5</sup>, Osvaldo Catalano<sup>1,6</sup>, Giancarlo Cerretto<sup>1,5</sup>, Andrea Giammanco<sup>1,7</sup>, Jon Gluyas<sup>1,8</sup>, Ivan Gnesi<sup>1,9,10,11</sup>, Marko Holma<sup>1,12,13,14</sup>, Tadahiro Kin<sup>1,15</sup>, Ignacio Lázaro Roche<sup>1,16</sup>, Giovanni Leone<sup>1,17</sup>, Zhiyi Liu<sup>1,18</sup>, Domenico Lo Presti<sup>1,19</sup>, Jacques Marteau<sup>1,20,21</sup>, Jun Matsushima<sup>1,2</sup>, László Oláh<sup>1,2</sup>, Natalia Polukhina<sup>1,22</sup>, Surireddi S. V. S. Ramakrishna<sup>1,23</sup>, Marco Sellone<sup>1,5</sup>, Armando Hideki Shinohara<sup>1,24</sup>, Sara Steigerwald<sup>1</sup>, Kenji Sumiya<sup>1</sup>, Lee Thompson<sup>1,25</sup>, Valeri Tioukov<sup>1,26</sup>, Yusuke Yokota<sup>1,2</sup> & Dezső Varga<sup>1,27</sup>

## Abstract

Muography takes advantage of the specific properties of cosmic-ray muons, relativistic leptons that are much heavier than electrons. Cosmic-ray muons have strong penetrating power and a relativistic nature, which means they can be used in a range of technologies, including imagery; positioning, navigation, timing (PNT); and secured communication in environments where conventional techniques are unavailable. As cosmic-ray muons are universally present on Earth, muographic measurements can be conducted in the same manner across the globe. Similar results have been produced independent of where measurements were taken. This has enabled the muographic field to grow and develop into a powerful tool for investigating natural phenomena, cultural heritage and PNT. This Primer is intended as an introductory article that introduces new and established muographic techniques. Case studies are provided, with examples from recent interdisciplinary advances. Data reproducibility and limitations are discussed, before finishing with an outlook of future developments.

## Sections

[Introduction](#)[Experimentation](#)[Results](#)[Applications](#)[Reproducibility and data deposition](#)[Limitations and optimizations](#)[Outlook](#)

<sup>1</sup>International Virtual Muography Institute, Tokyo, Japan. <sup>2</sup>The University of Tokyo, Tokyo, Japan. <sup>3</sup>Università degli Studi di Salerno, Salerno, Italy. <sup>4</sup>Fermi National Accelerator Laboratory, Batavia, IL, USA. <sup>5</sup>Istituto Nazionale di Ricerca Metrologica, Turin, Italy. <sup>6</sup>Istituto di Astrofisica Spaziale e Fisica Cosmica, Palermo, Italy. <sup>7</sup>Université catholique de Louvain, Louvain-la-Neuve, Belgium. <sup>8</sup>Durham University, Durham, UK. <sup>9</sup>CREAF, Centro Enrico Fermi, Roma, Italy. <sup>10</sup>INFN LNF gruppo di Cosenza, Frascati, Italy. <sup>11</sup>CERN, Geneva, Switzerland. <sup>12</sup>Muon Solutions, Oulu, Finland. <sup>13</sup>University of Oulu, Oulu, Finland. <sup>14</sup>Arctic Planetary Science Institute (APSI), Oulu, Finland. <sup>15</sup>Kyushu University, Fukuoka, Japan. <sup>16</sup>Laboratoire Souterrain à Bas Bruit (LSBB), Rustrel, France. <sup>17</sup>Universidad de Atacama, Copiapó, Chile. <sup>18</sup>Lanzhou University, Lanzhou, China. <sup>19</sup>Università di Catania, Catania, Italy. <sup>20</sup>Institute of Physics of the 2 Infinities (IP2I), Lyon, France. <sup>21</sup>MUODIM, Lyon, France. <sup>22</sup>Lebedev Physical Institute, Moscow, Russia. <sup>23</sup>Andhra University, Visakhapatnam, India. <sup>24</sup>Federal University of Pernambuco, Recife, Brazil. <sup>25</sup>The University of Sheffield, Sheffield, UK. <sup>26</sup>National Institute for Nuclear Physics (INFN), Naples, Italy. <sup>27</sup>Wigner Research Centre for Physics, Budapest, Hungary. ✉e-mail: [ht@eri.u-tokyo.ac.jp](mailto:ht@eri.u-tokyo.ac.jp)

## Introduction

Muography, in its broadest definition, is an academic and applied field of research that uses naturally produced elementary particles, cosmic-ray muons, to research natural objects and phenomena, as well as human society, infrastructure and culture. Four main muographic technologies have emerged (Fig. 1): imagery<sup>1</sup>; positioning and navigation<sup>3,4</sup>; time metrology<sup>5–7</sup>; and cryptography<sup>8,9</sup>. Muographic imagery (Box 1) is mainly used in radiographic applications to visualize the internal structure of large objects, by using the strong penetrability of high-energy muons emitted by cosmic rays<sup>1</sup>. Muometric positioning, navigation, timing (PNT) includes a muometric positioning system (muPS), cosmic time synchronization (CTS)<sup>5,6</sup> and cosmic time calibration (CTC)<sup>7</sup>. Muometric cryptographic protocols can be used as a secure authentication technique in wireless security, referred to as cosmic coding and transfer (COSMOCAT)<sup>8</sup>, and encryption key storage, referred to as COSMOCAT storage (COSMOCATS)<sup>9</sup>.

All muonic applications take advantage of seven properties of high-energy muons, which represent the majority of cosmic muon flux. These seven properties are strong penetration, enabling travel through a few kilometres of rock; velocities close to the speed of light in a vacuum; path lines that are practically straight, regardless of the substance traversed; virtually constant flux in all seasons and at all times of day; ubiquitous precipitation across the Earth; multiple generation near the tropopause; and arrival times with a true random number (TRN) nature.

Muons are the second most numerous secondary particles at sea level, after neutrinos<sup>10</sup>. However, unlike neutrinos, muons are charged particles and can be detected easily. An advantage of muography is that observations and measurements can be conducted without an artificial source for the probes or signals, as naturally occurring cosmic-ray muons are used. Most of these muons have high energies (multi-gigaelectronvolts and above) and kinetic energies greater than their mass. Consequently, although muons at rest are short-lived – intrinsic half-time 2.2  $\mu\text{s}$  – most cosmic muons survive long enough to cross the entire atmosphere due to relativistic time dilation. In addition, as muons are 207 times heavier than electrons, they lose much less energy via radiative loss. This means that muons travel further through matter than electrons with the same incident kinetic energy. In contrast to other cosmic particles with similar mass, such as pions, muons are insensitive to nuclear interactions. These features enable several applications, including radiographic imaging of large objects, ranging in size from nuclear waste barrels to volcanoes; muometric PNT; and wireless security in indoor, underground and underwater environments.

Another advantage is the unpredictable nature of muon arrival times. The arrival time distribution of cosmic-ray muons is entirely random: one event occurs completely independently of another event<sup>10</sup>. Combined with strong penetration, this enables cosmic-ray muons to deliver encryption keys to confined and secure locations, increasing the security of cloud-based authentication<sup>8</sup>.

This Primer is intended as an introduction to muographic imaging, muometric PNT and muometric encryption key distribution. The article aims to describe the muography technique and how muons can be used for applications in Earth and planetary sciences, as well as human, computer and social sciences. An overview of the method is provided throughout this Primer, with more specialized information available from refs. 11–13.

## Experimentation

This section provides an overview of the instrumental designs of muon imaging, PNT and cryptography experiments. It also introduces the fundamental background behind muographic experimentation.

## Muographic sources

Cosmic-ray muons are mainly generated as decay products of pions and kaons. Pions and kaons are produced by nuclear collisions of primary cosmic rays, protons and nuclei with nuclei in the atmosphere, according to the following processes:

$$\text{Charged pions: } \pi^{\pm} \rightarrow \mu^{\pm} + \nu_{\mu}(\bar{\nu}_{\mu}) \quad (-100\%) \quad (1)$$

$$\text{Charged kaons: } K^{\pm} \rightarrow \mu^{\pm} + \nu_{\mu}(\bar{\nu}_{\mu}) \quad (-63.6\%) \quad (2)$$

$$\text{Neutral kaons: } K_L \rightarrow \pi^{\pm} + e^{\pm} + \nu_e(\bar{\nu}_e) \quad (-40.6\%) \quad (3)$$

$$K_L \rightarrow \pi^{\pm} + \mu^{\pm} + \nu_{\mu}(\bar{\nu}_{\mu}) \quad (-27.0\%) \quad (4)$$

$$\text{Neutral kaons: } K_S \rightarrow \pi^{+} + \pi^{-} \quad (-69.2\%) \quad (5)$$

where  $\pi$ ,  $\mu$ ,  $\nu_{\mu}$ ,  $\nu_e$ ,  $K$ , and  $e$  respectively indicate a pion, a muon, a muon neutrino, an electron neutrino, a kaon and an electron. The superscripts (plus and minus) indicate the particle charge, and the subscripts (L and S) indicate the meson state of the kaon (long and short). The overline indicates an antiparticle. The numbers in parentheses refer to the branching ratio in the final state. Most secondary particles are generated at an altitude of  $\sim 15$  km. By assuming a pion and kaon generation spectrum of  $1.8 \times 10^4 E^{-2.7}$  nucleons  $\text{m}^{-2} \text{s}^{-1} \text{sr}^{-1} \text{GeV}^{-1}$  (ref. 9), the muon spectrum is approximated by Eq. (6), for the energy ( $E$ ) region where muon decay can be neglected ( $E > 100/\cos\theta$  GeV) and the Earth can be approximated to be flat ( $\theta < 70^{\circ}$ )<sup>9</sup>:

$$\begin{aligned} dI/dE d\Omega \approx & 0.14 E^{-2.7} [1/(1 + 1.1E \cos\theta/115 \text{ GeV}) \\ & + 0.054/(1 + 1.1E \cos\theta/850 \text{ GeV})] \text{ cm}^{-2} \text{s}^{-1} \text{sr}^{-1} \text{GeV}^{-1} \end{aligned} \quad (6)$$

where the first and second terms indicate the contribution of pions and charged kaons, respectively. A muon at rest decays with a half-time of  $\tau = 2.2 \mu\text{s}$ . However, as predicted by relativity, this decay constant extends as the muon accelerates to speeds ( $v_{\mu}$ ) close to the speed of light in a vacuum ( $c$ ). Consequently, the muon's survival probability ( $W$ ) and decay length ( $L$ ) are expressed by its path length ( $L_{\text{PATH}}$ ):

$$W = \exp(-L_{\text{PATH}}/L) \quad (7)$$

$$L = c\beta\gamma\tau = 3 \times 10^8 \text{ ms}^{-1} \times E/m \times 2.2 \times 10^{-6} \quad (8)$$

where  $E$  is the muon's kinetic energy and  $m$  is the muon mass.  $\beta$ ,  $\gamma$  and  $\tau$  are respectively  $c/v_{\mu}$ , the Lorentz factor and the muon's decay constant. As can be seen in Eq. (8), only relativistic muons can arrive at sea level.

As muons lose their energy in the atmosphere, muon flux energy is higher at higher altitudes. CAPRICE 94 muon measurements show that low-energy ( $< 2$  GeV) muon flux increases by a factor of five when atmospheric depth is half the value at sea level (500 hPa)<sup>14</sup>. The geomagnetic effect depends on the measurement latitude, with muon flux higher (up to a factor of two) at the equator and high-latitude regions<sup>15,16</sup>.

Muons lose energy through ionization and radiative processes, such as bremsstrahlung, direct pair production and photonuclear reaction. During ionization, muons frequently collide with electrons. A small fraction of the muon's energy is lost in each collision. Fluctuations in the muon's range are enhanced by radiative processes, where a muon loses a large random fraction of its energy. Critical energy is the

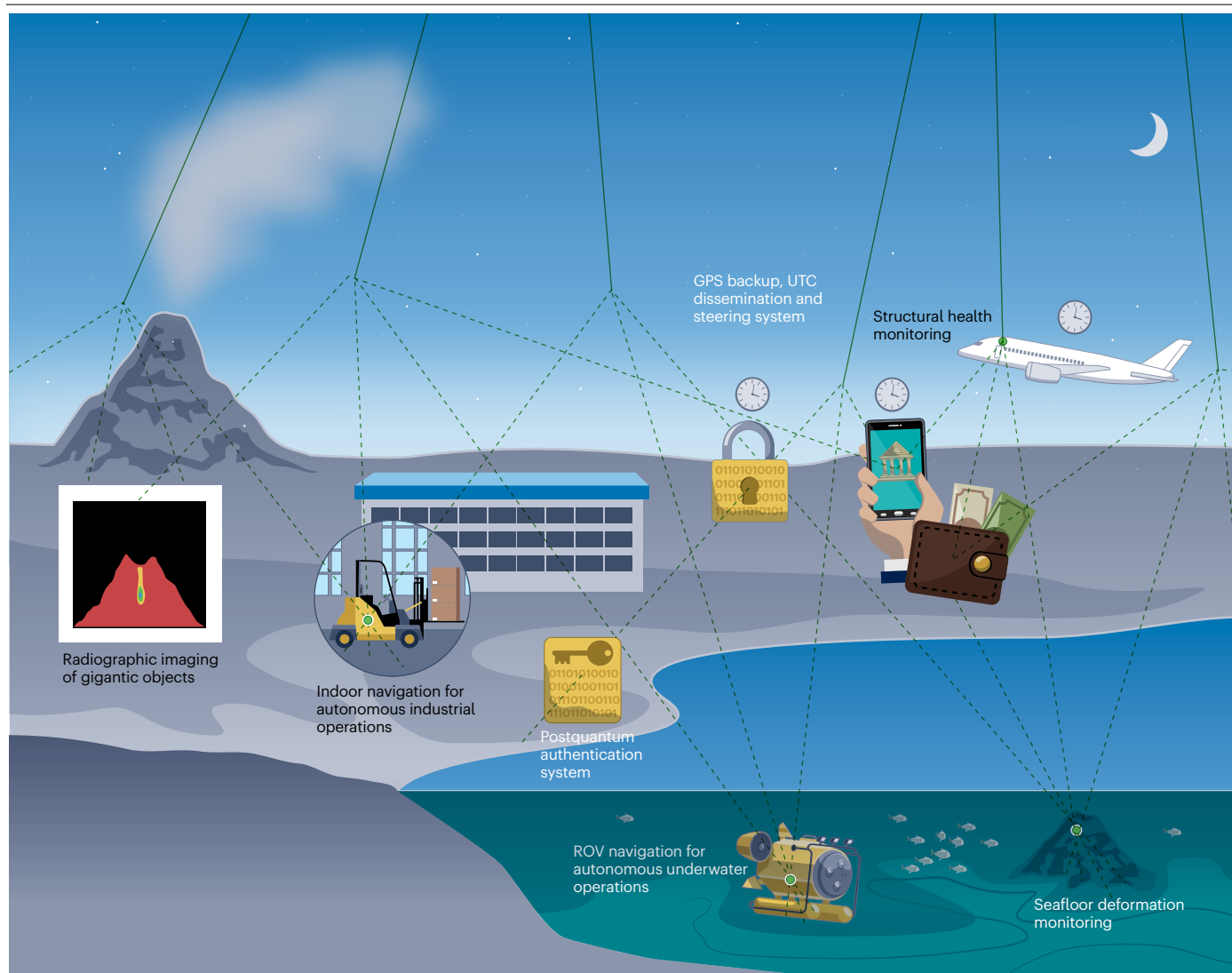


**Fig. 1 | Examples of imaging, positioning, navigation and timing, and cryptographic technologies in muography.** Applications include imaging of geological, historical and industrial objects; indoor, underground, underwater positioning and navigation; coordinated universal time (UTC) dissemination and

steering systems; wireless sensor networks; structural health monitoring; and tectonic seafloor deformation monitoring. GPS, global positioning system; ROV, remotely operated vehicle.

point where ionization loss equals bremsstrahlung loss. For example, the critical energy in air,  $\text{H}_2\text{O}$  and  $\text{SiO}_2$  is 1.11 TeV, 1.03 TeV and 708 GeV, respectively. Consequently, most cosmic-ray muons are subject to ionization processes. Vertical muons lose a few gigaelectronvolts of energy in the atmosphere before reaching the Earth's surface. This is because muon energy loss from air ionization is typically  $2\text{--}3 \text{ MeV g}^{-1} \text{ cm}^{-2}$ . The continuous slowing down approximation<sup>17</sup> is convenient for calculating the analytical muon range:

$$-dE/dX = a + bE \quad (9)$$

where the first and second terms indicate contributions from ionization and radiative processes, respectively. The parameters  $a$  and  $b$  depend on the material the muon is travelling through.

## Muographic instrumentation

All muography detectors, except those used for time-of-flight (TOF) muPS and CTS, share a common feature: they are designed to track cosmic-ray muons. These detector components are referred to as trackers. The azimuth angles ( $\phi$ ) and elevation angles ( $\theta$ ) of the incident particles can be computed by connecting a straight line between two vertex points  $(x_1, y_1)$  and  $(x_2, y_2)$  on planes in a space as follows:

$$\begin{aligned} \phi &= \tan^{-1}[(x_1 - x_2)/z] \\ \theta &= \tan^{-1}[(y_1 - y_2)/z] \end{aligned} \quad (10)$$

where  $z$  is the distance of the planes. The positioning resolution of the vertex points is  $(\Delta x, \Delta y)$  and gives the detector's angular resolution  $(\Delta\theta, \Delta\phi)$ . If these vertex points are registered within a sufficiently

## Box 1

### Terminology

The term tomography is sometimes misused when applied to muon-based imaging. Etymologically, the word tomography originates from cut or slice (ancient Greek)<sup>170</sup> and drawing. Unless the images acquired with muography are three-dimensional images, the term muon tomography should not be used. For example, the muographic images of volcanoes in ref. 1 are not tomographic (cross-sectional) images but projected images. The term muon radiography is also misleading, as the [definition of radiography](#) usually refers to X-ray imagery. When using the phrase muon radiography, clarification should be provided on whether X-ray-like imagery with muons or imagery with muonic X-rays is meant. Vague descriptions or the wrong use of terminology could potentially mislead researchers outside the muography community.

narrow time window, the same muon is identified as having passed through the tracker.

Scintillation detectors, gaseous detectors and Cherenkov detectors are real-time detectors that have high timing resolution. By contrast, nuclear emulsion detectors cannot be used for real-time reading of muographic data and are limited to imagery. The details of each detector type are discussed below. For brevity, other detector technologies less frequently used in muography, such as semiconductor detectors, are not described.

**Muographic imagery.** Although imagery does not require sub-microsecond time resolution, the muographic instrumentation needs precise tracking capabilities. Detectors with better angular tracking resolution ( $\Delta\theta$ ,  $\Delta\phi$ ) can acquire muographic images with better definition. Scintillation detectors, gaseous detectors, Cherenkov detectors and nuclear emulsions have been used for muographic imagery. Photons are generated in plastic scintillator strips<sup>18–20</sup> or scintillation fibres<sup>21</sup>. These strips and fibres are configured vertically and horizontally to form X–Y position-sensitive detectors (Fig. 2a). The generated photons are subsequently detected by photodetectors. Muons are tracked by connecting two or more vertex points defined within two or more position-sensitive detectors (Fig. 2b). Photomultiplier tubes<sup>18</sup>, multi-anode photomultiplier tubes<sup>19</sup> and silicon photomultipliers<sup>20</sup> have been used as photodetectors. Scintillation detectors yield timing data for individual muon events. Placing a radiation shield between position-sensitive detectors means the system can reject the electromagnetic component of the cosmic-ray flux – the electrons and photons – and estimate the muon's momentum via multiple-coulomb scattering<sup>18</sup>. Although rectangular scintillators, which have a rectangular cross-sectional shape, are commonly used, a triangular scintillator extrusion is favoured if more precise point resolution of the detector planes is required. Scintillation light produced by charged particles travelling to the photodetector is transported by wavelength shifting fibres embedded into each strip. Typically, when a muon passes through a counter, it deposits charge in two adjacent triangular extrusions. A charge weighting algorithm, which determines the relative amount of ionization deposited in the two strips, can achieve a point resolution better than 1 mm (ref. 22). Extruded plastic

scintillator detectors, which were first used for geophysical studies<sup>23</sup>, can be assembled into very large arrays of hundreds of square metres. Relatively large scintillator arrays have been deployed in the volcano imaging project<sup>24</sup>.

Gaseous detectors commonly used for muographic imagery have a two-dimensional array of wires<sup>25–28</sup> or a mesh<sup>29</sup> applied at high voltage. A conceptual view of gas amplification near wires is shown in Fig. 2c. The chamber is filled with a carefully chosen gas, such as an argon/methane mixture. Gaseous detectors can be used when a time-dependent, high-resolution measurement is required over a large surface. Disadvantages of gaseous detectors are the complicated tracking systems and the need for a gas supply. Dedicated optimization<sup>30</sup> can minimize gas consumption and reduce the number of gas cylinders attached to the system. Contemporary gaseous muography systems are more robust and mechanically and environmentally stable<sup>31,32</sup> than early, laboratory-based systems.

Muons can also be tracked using Cherenkov light emitted by relativistic cosmic-ray muons in the atmosphere<sup>33,34</sup>. Cherenkov muon ring images contain all of the information needed to reconstruct a muon's direction and energy. This is because all relativistic charged particles produce Cherenkov light if they travel faster than  $c/n$ , where  $c$  is the speed of light and  $n$  is the refraction index ( $n \geq 1$ ). The muon energy is determined by the following formula:

$$E_{\mu} \text{ (GeV)} = 0.105 \cdot [(1 - (\cos\vartheta)/n^2)]^{1/2} \quad (11)$$

where  $\vartheta$  is the emission angle<sup>9</sup>. These measurements cannot be performed in daylight, but clouds and far-away trees do not affect observations.

Nuclear emulsions<sup>35</sup> have been used in many static muographic imagery applications. They do not have a time resolution and do not require electric power. Each muon crossing a film (50–100  $\mu\text{m}$  thick) of AgBr crystals in a gel leaves a trail of  $\text{Ag}^+$  ions. As a result, a three-dimensional image is formed that fully tracks all muons passing through the film from production to development. Figure 2d shows the basic concepts of a modular muon telescope based on nuclear emulsions. Emulsion readout systems and data analysis frameworks are established and can be used in muographic imagery<sup>36–46</sup>. Nuclear emulsions are best operated above 5 °C and below 30 °C, as the emulsion melts at  $\sim 40$  °C. For environments with temperatures outside this range, other detectors are needed.

**Positioning, navigation, timing and cryptography.** Muographic detectors used for PNT and cryptography need an absolute timestamping function. As scintillation detectors have higher time resolution than gaseous detectors, the muon's TOF and arrival time can be precisely measured<sup>2</sup>. Combining a photomultiplier tube and constant fraction discriminator, sub-nanosecond timing precision can be achieved<sup>2,9</sup>. Muons are directional and have low flux. This limits applications of muPS, CTC and COSMOCATS as the time required to acquire useful data is inversely proportional to the solid angle formed by the reference and receiver.

The muometric PNT system does not have an absolute clock. As a result, standard time needs to be introduced using the global positioning system (GPS) or coordinated universal time (UTC( $k$ )) as a timestamp of the absolute time. These timestamps are used as time information for PNT and encryption keys for cryptography. Muometric PNT has been performed by connecting a GPS disciplined oscillator<sup>3,4,6–8</sup> (Fig. 3). A 10-MHz pulse output from the GPS is fed to the event counter, and



the time differences between the GPS pulses and the muometric PNT pulses measured using a time to digital converter (TDC). The receiver detector is equipped with a local clock, so the absolute time at the reference detector can be transmitted even if the receiver detector is in a GPS-denied environment, such as underground. Oven-controlled crystal oscillators have been used as the local clock<sup>3,4,6–8</sup>. The local clock drifts over time and needs to be frequently calibrated with PNT signals from the reference detector. If the calibration time interval is sufficiently shorter than the drift timescale, drift can be ignored<sup>6</sup> and the receiver detector will continuously output the absolute time.

If muons are used for steering local clocks, altitude and geolocation-dependent variations in flux can affect the clock calibration frequency. As clocks generally drift, higher or lower calibration frequencies result in better or worse clock granularity. For navigation, muon flux is proportional to the positioning signal update rate. Near ground level, however, this rate does not vary by enough orders of magnitude for real-time navigation. As a result, positioning performance is not expected to be significantly influenced by muons in this region. For example, due to the limited flux of cosmic muons, the muometric

positioning information needs to be interpolated using inertial measurement units for practical navigation. By contrast, the positioning update rate is substantially upgraded for navigation in high altitudes. Such high muon flux could be used for high-precision applications, such as automated robotic operations in cargo planes.

## Results

Information that can be obtained by muography includes time-sequential images of natural phenomena and cultural heritage, or precise arrival times for PNT and cryptography. This section discusses general muography simulation techniques, plus specific modelling and data preparation methods for imagery, PNT and cryptography.

### Muography simulations and data analysis

A typical Monte Carlo simulation chain begins by generating muons with realistic angular and momentum distributions. Approaches range from single-particle parametrizations to *ab initio* computations of the extended air shower (EAS) development, for example in the CORSIKA<sup>47</sup>, CRY<sup>48</sup>, and AIRES<sup>49</sup> programs.

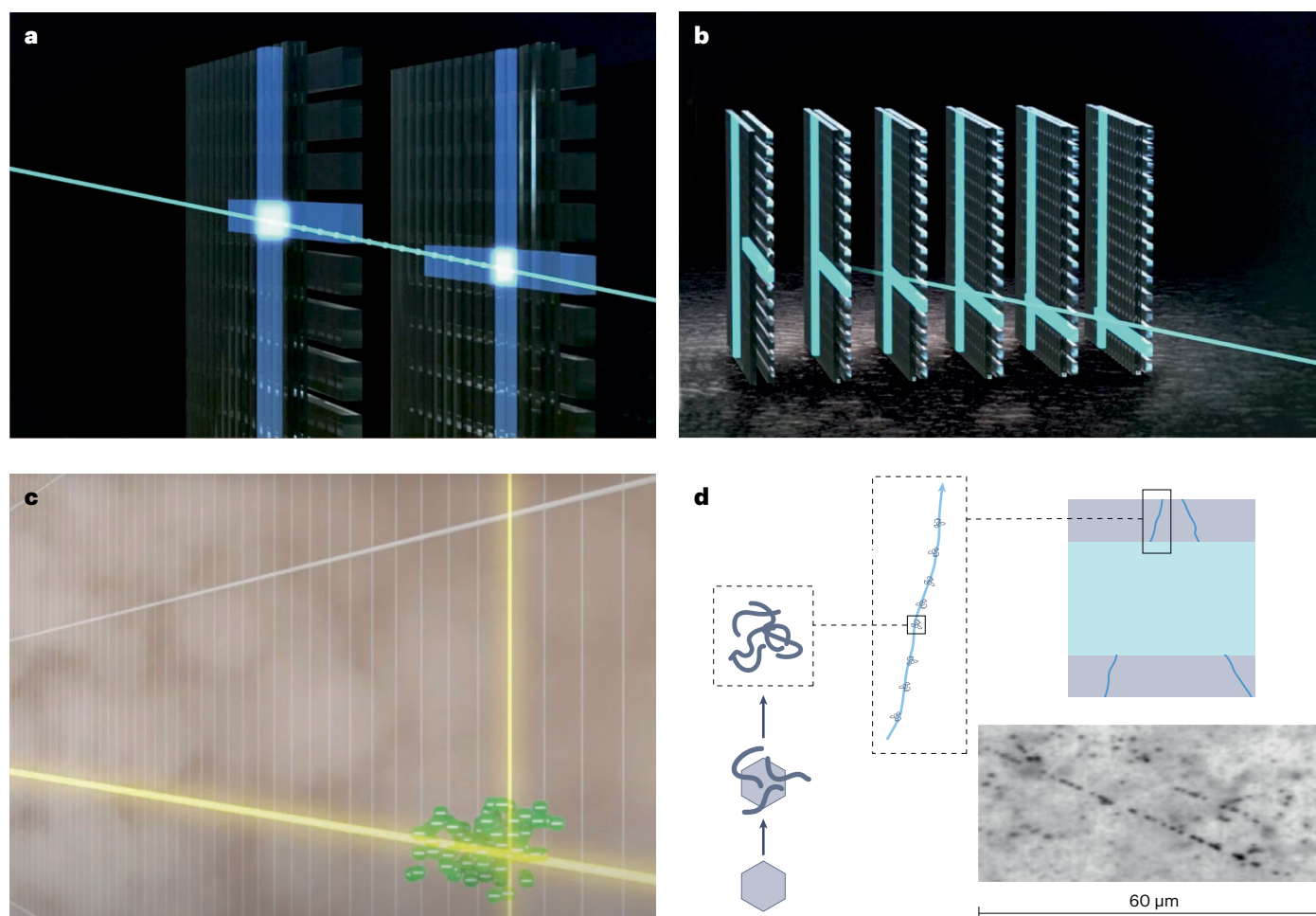


**Fig. 2 | Instrumentation used for muographic imagery. a**, X–Y position acquired from vertically and horizontally configured scintillator strips. Blue line indicates the trajectory of a muon. **b**, Muon tracker with multiple position-sensitive detectors. **c**, Conceptual view of gas amplification near wires. Green dots and yellow lines respectively indicate the particles ionized by the incident

muons and the wires fired by these ionized particles. **d**, Muon tracks recorded in nuclear emulsions. Silver filaments grow from the sensitized sites of an AgBr crystal touched by a charged particle. A trail of developed grains marks the track of an ionizing particle in emulsion films. An optical microscope image of a track is shown.

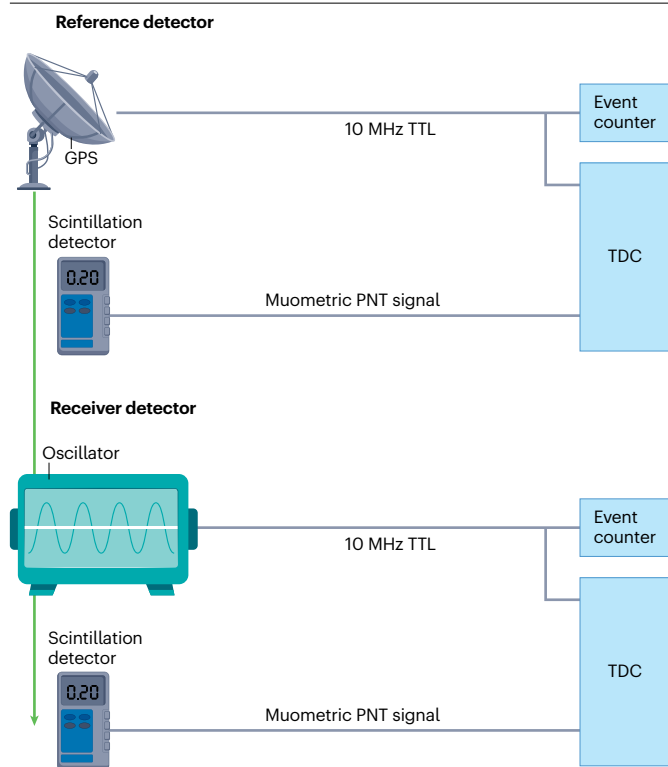


**Fig. 3 | Instrumentation used for muometric positioning, navigation and timing and imaging and cryptography.** A global positioning system (GPS) is used for positioning and timing of the reference detectors, which are subsequently transmitted by the muon (green arrows) to the receiver detector located in a GPS-denied environment. PNT, positioning, navigation, timing; TDC, time to digital converter; TTL, transistor–transistor logic.

The most crucial step in muography simulations is the passage of muons through dense material. GEANT4 (ref. 49) is a framework that can accurately simulate particle interactions through matter in the energy range relevant to muography. However, GEANT4 becomes too computationally expensive at large volumes. As a result, parametric simulations have been developed to reduce computational processing times, while preserving a fair level of accuracy<sup>50</sup>. For muographic imaging, another approach is to use backward Monte Carlo, as implemented in PUMAS<sup>51</sup>, where the simulation runs from the detector to the sky. This means no time is wasted simulating muons outside the acceptance range. However, background events are not included in this strategy, although this is not a problem if the muography set-up has efficient radiation shielding.

The geometry and detector response also need to be simulated. Simple parametrizations of detector efficiency can be sufficient in many cases. However, when data sets are large and high-precision imaging is the goal, approximations in the detector simulation may result in statistically significant biases in the images obtained; in those cases, detailed simulation programs such as GEANT are typically used<sup>50</sup>.

## Muographic imagery

**Modelling.** Some muons stop in their path through an object, depending on the object's size and density structure. If the exterior shape and average density of the target volume is given, the areal density along the

muon path ( $x$ ) can be calculated. From this areal density, the minimum energy ( $E_c$ ) required for a muon to penetrate and escape the volume is determined using Eq. (9). By integrating Eq. (6) from  $E_c$  to infinity, the integrated muon intensity ( $\Phi$ ) recorded in each pixel of the muographic image is obtained:

$$\Phi = \int_{\phi}^{\phi+\Delta\phi} \int_{\theta}^{\theta+\Delta\theta} \int_{E_c}^{\infty} I(E, \theta, \phi) dE d\theta d\phi \quad (12)$$

where  $\theta$ ,  $\phi$ ,  $\Delta\theta$  and  $\Delta\phi$ , are the zenith angle, azimuth angle, zenith angular pixel size and azimuth angular pixel size, respectively.

**Data preparation.** Inversely, by measuring  $\Phi$  after passing through the target volume, raw data can be acquired to derive  $x$  in each pixel. As can be seen in Eqs. (6) and (12), the flux available for muographic imagery is proportional to the size of the detector. Imaging a large structure – such as a volcano or the Great Pyramid of Giza – requires large-scale muon detectors to collect data in an acceptable amount of time. This is because there are rate limitations from the cosmic-ray muon flux, imaging is required over many different angles throughout the structure and sufficient data need to be accumulated per effective voxel to minimize noise and maximize image fidelity. Generally, standard cargo containers<sup>22</sup> and prefabricated buildings<sup>28</sup> are used to house the large detector arrays, as this is easy to implement and cost-effective.

Eventual mass production and commercialization will require the muography detector to be compacted<sup>52–56</sup>. However, for a target with a given size, smaller detectors require more time to prepare the raw data. Radiography is a standard technique for investigating smaller-sized target volumes, but muographic imagery may be a cheaper solution for conditions where artificial radiation sources cannot be used. Such techniques could investigate objects by locating cosmic muon interactions in the target volume from scattering angles<sup>57–59</sup> and secondary radiation emission<sup>60</sup>.

## Muometric positioning, navigation and timing

PNT is used in social operations, ranging from financial transactions to homeland security. Current methods rely on GPS and other global navigation satellite systems (GNSSs). Satellite-based positioning relies on low-power and unencrypted signals, meaning these methods are susceptible to intentional and unintentional disruption. An alternative PNT system is in demand as a GPS back-up to increase the resiliency of critical infrastructure and reduce GPS vulnerabilities, as demonstrated by the [US Department of Homeland Security PNT Program](#).

**Modelling.** Most cosmic-ray muons have a velocity close to the speed of light in vacuum, meaning  $\gamma$  is much larger than 1. This relativistic nature enables the time ( $T$ ) required for cosmic-ray muons to travel a distance between two detectors ( $D$ ) to be approximated as:

$$T = Dc^{-1} \quad (13)$$

regardless of the material traversed.

This is a key concept of muPS, a technique similar in principle to GPS. TOF muPS requires three or more reference detectors to form the reference coordinates (Fig. 4a, left), instead of the satellites used for GPS. The receiver detector defines the relative position within this coordinate system by the following relationship:

$$L_i^2 = (x_i - x_p)^2 + (y_i - y_p)^2 + (z_i - z_p)^2 \quad (14)$$

where  $L_i$  is the geometrical distance between the  $i$ th reference detector located at  $(x_i, y_i, z_i)$  and the receiver detector located at  $(x_p, y_p, z_p)$ .

Vector muPS (Fig. 4a, right) is another wireless muometric positioning technique<sup>61</sup>. Using the directional vectors ( $\mathbf{a}(a_x, a_y, a_z)$ ) of incoming muons at the reference, the two-dimensional position of the receiver ( $x_{\text{rec}}, y_{\text{rec}}$ ) is defined by fixing the parameter ( $s$ ) of one vector component ( $z_{\text{ref}} + sa_z = D$ ) so that:

$$\begin{aligned} (x_{\text{rec}}, y_{\text{rec}}, z_{\text{rec}}) &= [x_{\text{ref}} + (z_{\text{rec}} - z_{\text{ref}}) \tan\theta, \\ y_{\text{ref}} + (z_{\text{rec}} - z_{\text{ref}}) \tan\theta \tan\phi, (z_{\text{rec}} - z_{\text{ref}})] \\ &= (x_{\text{ref}} + D \tan\theta, y_{\text{ref}} + D \tan\theta \tan\phi, D) \end{aligned} \quad (15)$$

where  $(x_{\text{ref}}, y_{\text{ref}}, z_{\text{ref}})$  is the muon hitting positions on the reference.  $\theta$  and  $\phi$  are the zenith angle and azimuth angle of the incident muons, respectively.

The three-dimensional position of the receiver is approximated as the position where the two muon trajectories ( $x_{\text{ref1}} + sa_x, y_{\text{ref1}} + sa_y, z_{\text{ref}} + sa_z$ ) and ( $x_{\text{ref2}} + tb_x, y_{\text{ref2}} + tb_y, z_{\text{ref}} + tb_z$ ) approach closest to the receiver. The positioning accuracy comes from the angular resolution of the reference detectors and is linearly degraded as a function of the distance between the reference and the receiver. The advantages of vector muPS are that fewer muon tracks are required for positioning and precise time synchronization between the reference and receiver is not needed.

There are two types of muometric time synchronization techniques: time synchronization using EAS particles, called CTS<sup>5,6</sup>, and time synchronization using the muon's TOF, called CTC<sup>7</sup>. CTS measurements are modelled using the simultaneity characteristics of remote EAS particles. EASs are cascades of secondary particles – electromagnetic and hadronic cascades – generated by high-energy interactions of primary cosmic rays with atmospheric nuclei. Modelling mainly involves estimating the EAS time structure while varying the path length and velocity of the secondary particles. The longitudinal spread limits the time synchronization precision of CTS<sup>5</sup>. The difference in arrival time is generally smaller than 100 ns when detected on the ground, enabling long-term wireless synchronization of local clocks in the EAS shower disc (Fig. 4c). CTC uses the cosmic-ray muon's well-known travelling speed (Eq. (12)) and nodal distance values to calibrate local clocks within a sensor network<sup>7</sup> (Fig. 4d).

**Data preparation.** Two device configurations are used for muometric positioning and navigation: wired<sup>4</sup> and wireless<sup>3,4</sup>. In a wired system, time synchronization between the reference and receiver detectors is obvious (Eq. (13)) with only three variables<sup>2</sup>. By contrast, a wireless system requires time synchronization with local clocks that have intrinsic frequency drift, causing a time offset error ( $\Delta t$ ) between the reference and receiver clocks. In a wireless system, Eq. (13) has one more variable:

$$L_i^2 = (x_i - x_p)^2 + (y_i - y_p)^2 + (z_i - z_p)^2 + s^2 \quad (16)$$

where  $s (= c_0 \Delta t)$  is the pseudo-length from time offset at the receiver detector<sup>3</sup>. For wireless navigation, four or more reference detectors are required to prepare raw data.

Whereas CTS can synchronize all clocks inside the area covered by the shower disc (thousands of square metres) with a nodal distance of 180 m, CTC can synchronize clocks in much smaller areas<sup>7</sup>. This is because the parameter  $D$  in Eq. (12) cannot be too large. As a result,  $\Delta\theta$

and  $\Delta\phi$  in Eq. (11) need to be large enough to measure the muon's TOF in a realistic timeframe. To prepare data with CTC, the nodal distance must be reasonably short.

## Cryptography

**Modelling.** There have been attempts to generate true random numbers (TRNs) using the muon's arrival times<sup>62</sup> or energies deposited at the detector. However, the cosmic muon flux intensity is too small to compete with the generation efficiency of current TRN generators, which can generate  $2.5 \times 10^{14}$  TRNs per second<sup>63</sup>. Therefore, it was thought that cosmogenic TRNs have no practical applications in modern communication systems. Muometric cryptography compensates for low-rate TRN generation with safe TRN transfer capabilities in a common key cryptosystem. Muometric cryptography enables the same TRNs to be shared in different locations<sup>8</sup> (Fig. 4b). Modelling muographic cryptography involves estimating key generation rates with a given geometrical configuration of the detector set-up calculated with Eq. (12).

Security issues during data transfer are being considered to prevent cyber-attacks<sup>64</sup>. Public key cryptography is highly rated for its robustness. Security is enhanced by incorporating the complex calculation processes into the keys. However, it is not suitable for exchanging large amounts of information, because data encryption requires extra processing power. As information traffic increases, the amount of processing power also increases. Another disadvantage is that a quantum computer will be able to crack public key cryptography, such as Rivest–Shamir–Adleman cryptosystem-based encryption. The cryptographic community needs to develop robust methods and algorithms for post-quantum cryptography before quantum computers become widespread<sup>65</sup>. Common key cryptography does not have these drawbacks. However, the same key is used for both sender and receiver, which means keys need to be physically transferred. They need to be delivered safely, which takes time and effort to reduce the risk of encrypted contents being leaked. COSMOCAT mitigates this risk by removing the process of sending keys. Additionally, COSMOCAT generates true random number keys, which quantum computers cannot cryptanalyse and crack in a realistic timeframe.

**Data preparation.** With COSMOCAT, the sender creates an encryption key from a random number derived from the time the muon was detected. The sender then encrypts and transmits the data. High-energy muons travel close to the speed of light, regardless of where they are – indoors or outdoors, above ground or underground. The receiver can estimate the sender's detection time based on the muon's TOF between sender and receiver. From this, the same encryption key can be generated, with no physical exchange of keys via conventional information traffic, such as WiFi.

## Applications

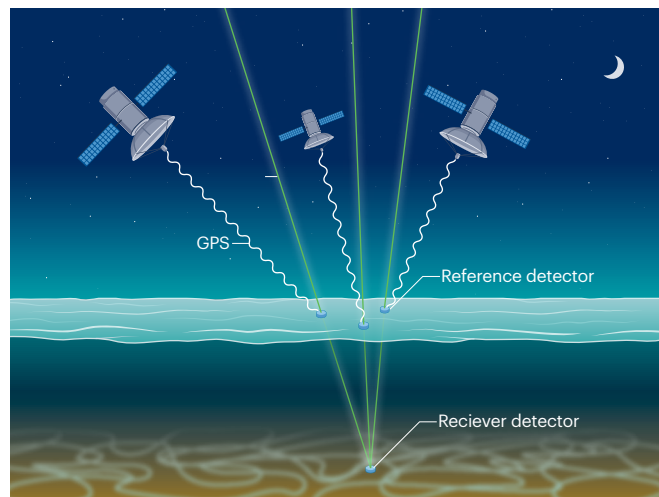
Muography addresses issues relevant to multiple sciences and industries. New tools and ideas continue to emerge from public and private laboratories. In this section, applications of muographic imagery, muometric PNT and muometric cryptography are introduced. Due to space limitations, this Primer only discusses a few directions where this research may lead.

### Muographic imagery

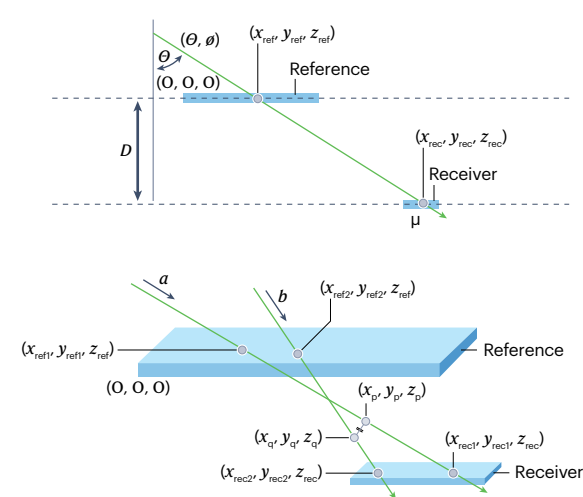
There are several potential applications of muographic imagery. These include geological investigations of volcanoes<sup>1</sup>, landslides, mines<sup>66,67</sup>

## a muPS

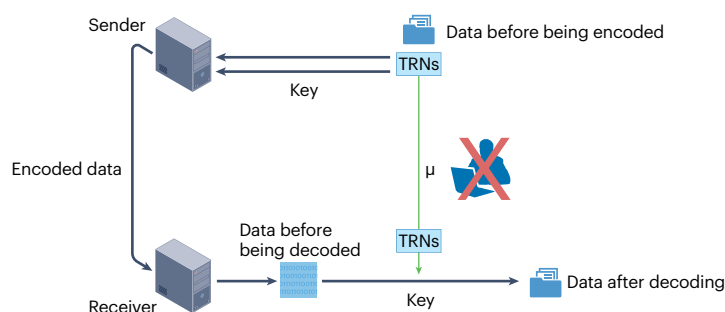
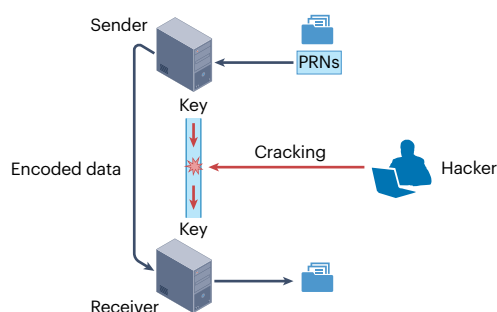
### Time-of-flight muPS



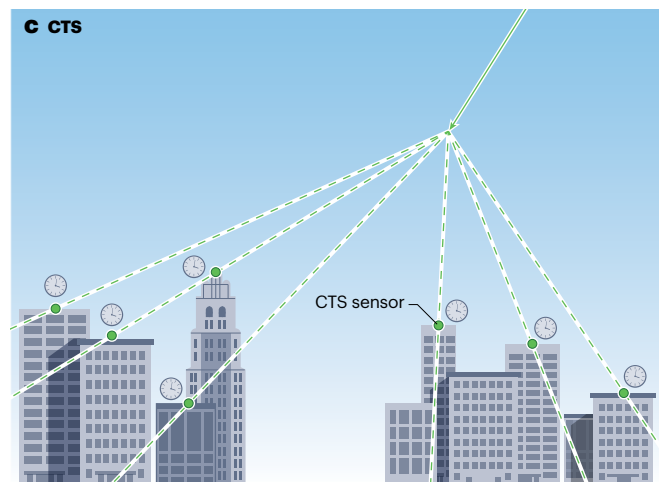
### Vector muPS



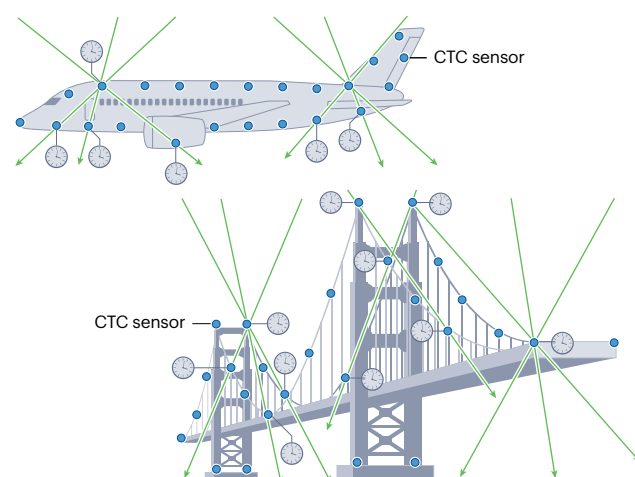
## b COSMOCAT



## c CTS



## d CTC



and glaciers<sup>68</sup>; non-destructive testing, evaluation and monitoring of industrial plants and civil engineering structures, such as electric furnaces, blast furnaces<sup>69</sup>, nuclear reactors<sup>70,71</sup>, railway tunnels<sup>72</sup>, underground pillars<sup>73</sup> and check valves<sup>74</sup>; and non-destructive surveys of cultural heritage, such as pyramids<sup>75,76</sup>. Not all applications can be discussed here, but several successful examples are briefly introduced.

**Volcanism.** An important application of muographic imaging is to visualize the internal structure of volcanoes. Density is a physical quantity used to understand volcanic activities. Density variations are readily interpreted as mechanical changes occurring inside volcanoes. Time-sequential muographic density maps indicate local-scale geodynamics. Muographic density maps of mountains were acquired in the mid-1990s<sup>77,78</sup> and the first muographic density maps of an active



**Fig. 4 | Muometric positioning, navigation, timing and cryptography.**

**a–d**, Principles of a muometric positioning system (muPS) (panel **a**), cosmic coding and transfer (COSMOCAT) (panel **b**), cosmic time synchronization (CTS) (panel **c**) and cosmic time calibration (CTC) (panel **d**). Panel **a** (left) shows the principle of time-of-flight (TOF) muPS. The three-dimensional positions of three or more reference detectors are defined with a global positioning system (GPS), and the three-dimensional position of the receiver detector is defined within the coordinate defined by these reference detectors. Panel **a** (right) shows the principle of vector muPS. The two-dimensional position of the receiver is determined as an intersection point between the muon trajectory determined by the reference detector and the horizontal plane where the receiver detector is located (upper panel). The three-dimensional position of the receiver is determined based on the three-dimensional position where

two muon trajectories approach closest (lower panel).  $(x_{\text{ref}}, y_{\text{ref}}, z_{\text{ref}})$  are the muon hitting positions on the reference;  $(x_{\text{rec}}, y_{\text{rec}}, z_{\text{rec}})$  are the muon hitting positions on the receiver;  $(x_p, y_p, z_p)$  and  $(x_q, y_q, z_q)$  are respectively the three-dimensional position where the two direction vectors (**a** and **b**) approach closest. Panel **b** shows the conventional common key cryptosystem (left panel) and the COSMOCAT-based common key cryptosystem (right panel). Pseudo-random numbers (PRNs) and true random numbers (TRNs) are used for keys for encoding the data. Panel **c** shows intra-city time synchronization. Dashed lines indicate extended air shower (EAS) particles.  $D$ , distance between two detectors. Panel **d** shows time synchronization of sensor networks in an aircraft (top) and a bridge (bottom). Green arrows in panels **a–d** indicate cosmic-ray muons. Part **a** (left), image courtesy of H.K.M.T. Part **a** (right) adapted from ref. 61, Springer Nature Limited. Part **b** adapted from ref. 8, CC BY 4.0.

volcano were acquired at Mount Asama, Japan<sup>79</sup> in 2007. Following this initial demonstration, similar density maps were acquired for volcanoes in Japan, including Usu<sup>80</sup>, Showa-Shinzan lava dome, Asama<sup>79,81,82</sup>, Izu peninsula<sup>83</sup>, Omuroyama<sup>84</sup>, Unzen<sup>85</sup>, Shinmoedake<sup>86</sup>, Sakurajima<sup>87,88</sup> and Satsuma-Iwojima<sup>89,90</sup>; in France, for La Soufrière<sup>91</sup> and Puy de Dome<sup>92</sup>; and in Italy for Etna<sup>93</sup>, Vesuvius<sup>24</sup> and Stromboli<sup>94</sup>. Volcanological targets that can be imaged include magma movements<sup>90</sup>, plug formation<sup>88</sup>, crater floor collapse<sup>93</sup>, hydrothermal deformation<sup>95</sup> and tephra deposition and erosion<sup>96</sup>. Muography data can be combined with gravimetry<sup>97–99</sup>, seismotomography<sup>100</sup> and satellite-based interferometric synthetic aperture radar<sup>88</sup>. Knowing the magma rise evolution process in the conduit of a volcano as early as possible buys critically important time for initiating alarm and evacuation protocols. Although the muographic imaging technique is limited to horizontal ranges of 2–3 km, and is only applicable to near-surface depths, it has been applied to study lava dome formation<sup>80</sup> and collapse<sup>83</sup>, magma ascent and descent<sup>90,101</sup> (Fig. 5a), the vulcanian explosion mechanism<sup>79</sup>, magma convection<sup>102</sup> and the tectonic history of peninsula formation<sup>83</sup>.

**Cultural heritage.** Many cultural heritage structures are well suited for muographic imagery. Muographic surveys have been conducted at cultural heritage structures in Egypt, Italy, China, Indonesia, Japan and Mexico. Archaeological sites that have been explored include the Giza pyramids<sup>75,103</sup>, the imperial mound of Japan<sup>104</sup>, the Xi'an city wall in China<sup>105</sup>, the Prambanan Temple in Indonesia<sup>106</sup> and the caves of Mt. Echia, which are ancient settlement ruins in Naples<sup>107,108</sup>.

As an example, some investigations have searched for interior structural anomalies, including large voids, in cultural heritage structures<sup>75,102,104,105</sup>. An elongated void inside Khufu's pyramid in Egypt was first reported in 2017 by a muography team<sup>75</sup>. Additional data have since been collected to characterize the void, leading to the conclusion that the shape is consistent with a corridor-like structure ~9 m in length and a transverse section of ~2 m × 2 m (ref. 76). These conclusions were supported by ground-penetrating radar measurements and ultrasonic testing<sup>109</sup>. Visual inspection with an endoscope (bore-scope) provided conclusive evidence of the corridor first observed by muographic imaging. It is speculated that the chamber may have been created to redistribute the pyramid's weight around the entrance, or an undiscovered chamber, as discussed in a [news article about the hidden corridor](#).

Other findings have brought new historical and archaeological implications. For example, imaging of a crack formation process inside the imperial mound of Japan indicated that mound deformation was caused by translational collapse. These findings, along with trench

survey data, indicated an intrinsic problem with foundation stability before the 1596 Fushimi earthquake<sup>104</sup>. It was concluded that changes in the foundation due to shaking from a major earthquake may have produced the large-scale burial mound collapse. Additionally, the muographically estimated total weight of the pyramids<sup>110</sup> was compared with ancient records on the construction and building timescales of fourth-dynasty pyramids<sup>111</sup>. Muographic weight estimations are better than measuring cubic units of exposed masonry, which can be inaccurate for determining the scale of the building process. Along with other archaeological evidence, it was concluded that before the Giza projects, ancient Egyptian architects could not complete a pyramid during the Pharaoh's reign. However, for the Giza projects, pyramids could be built faster and were finished within the Pharaoh's reign<sup>111</sup>.

**Underground imagery of groundwater, mining and underground construction.** In 2011, muographic imaging was used to monitor groundwater dynamics in a mechanically fractured zone inside a seismic fault<sup>112</sup>. Following this work, muographic survey and monitoring activities were used to search for water resources<sup>113</sup>, prevent landslides and monitor debris flows of gravity-driven, rapidly moving materials composed of rock debris and water<sup>96</sup>. The main goal of the Tomographic Research of Underground and large Structures with Muographic Expertise (TRUST-ME) project, carried out by the Low Background Noise Underground Research Laboratory of Rustrel (LSBB), is to characterize the dynamics of water transfer processes in the critical zone and their cycles in the Fontaine-de-Vaucluse region. The project also aims to monitor large water storage infrastructures to enhance safety and operational efficiency. Both objectives address a critical and important societal challenge of sustainable water management<sup>113</sup>.

Another application of underground muographic imagery is in mining investigations. Muographic imaging has promising potential for detecting ore deposits<sup>66</sup> and in open pit or underground tunnelling and mining projects<sup>114</sup>. These include geological mapping, void detection, drilling and tunnel optimization. Muographic imagery may also improve human safety by detecting and monitoring faults. For such applications, muography can monitor unseen structures in front of a tunnel-boring machine. In addition, the extent of collapses in underground environments may be determined with one or several muon detectors in a deeper tunnel. Further applications in rock mechanics and engineering may be developed in the future<sup>115</sup>.

Unexpected geological features present challenges that can only be overcome with real-time adaptations during tunnel-boring operations, which can be expensive. Detecting such anomalies before physically encountering them requires real-time density analysis.

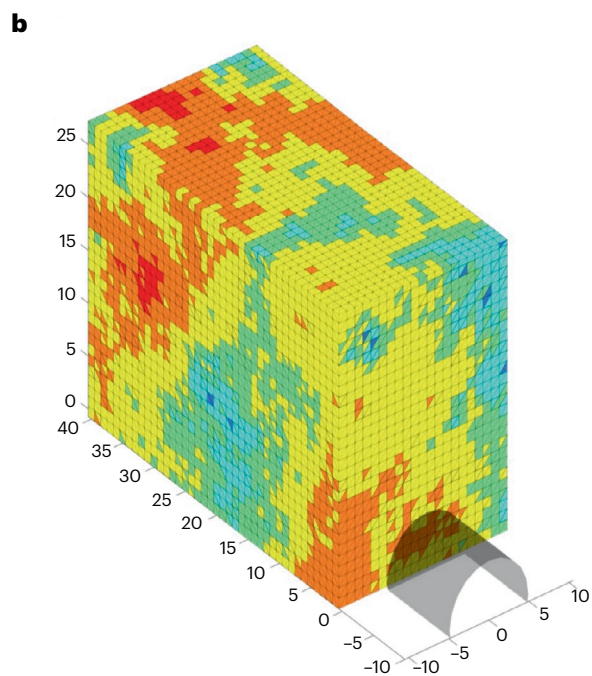
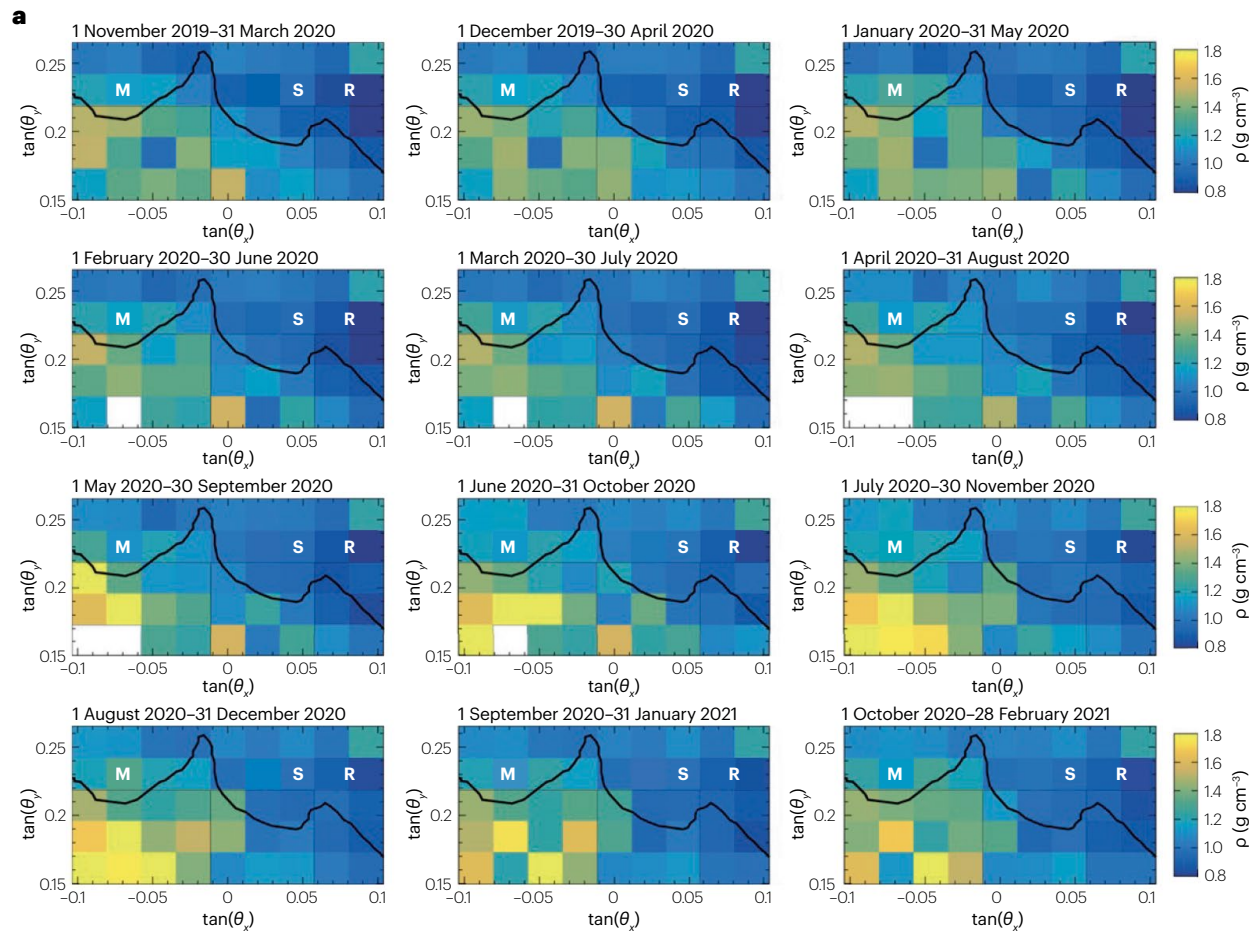


**Fig. 5 | Applications of muographic imagery.** **a**, Time-sequential density images of Sakurajima volcano as an example of time-sequential imagery. Average density ( $\rho$ ) values are plotted for the crater region of the volcano as a function of horizontal ( $\theta_h$ ) and elevation ( $\theta_e$ ) angles. The labels M, S and R respectively indicate Minamidake crater, Showa crater and reference region of Sakurajima

volcano. Each data plot shows a period of 5 months between 1 November 2019 and 28 February 2021. **b**, Online three-dimensional density reconstruction in front of a tunnel-boring machine as an application example of tomography<sup>116</sup>. Each cube is 1 m<sup>3</sup> in volume. Part **a** reprinted from ref. 88, CC BY 4.0.

Muography can provide this via continuous three-dimensional reconstruction of the geology in front of a tunnel-boring machine. Since 2017, the Lyon team, France and its start-up **MUODIM** developed the concept and original reconstruction algorithms for drilling the Grand Paris Express subway network, using scintillator-based muon detectors<sup>116</sup>. The muon detector is designed to image structures as it moves forward. As a result, the muon flux crossing a geological object measured by the telescope will have different directions with respect to time. These can be combined to generate three-dimensional density estimates (Fig. 5b).

**Atmospheric and oceanographic sciences.** Muography was recently extended to atmospheric and oceanographic objects, such as tropical cyclones<sup>117</sup> and tsunamis<sup>118</sup>. **MUOGRAPHIX** installed a hyper-kilometric submarine deep detector (HKMSDD) in the **AquaMuography Research Facility** located inside the trans-Tokyo Bay expressway underwater tunnel to detect offshore tidal variations<sup>119</sup>. Underwater tunnels enable researchers to exploit the larger muon flux from vertical directions (Eq. (6)). However, installing HKMSDDs into underwater tunnels is not the only way to monitor tide levels. They can also be installed inside near-shore urban underground spaces and land lying below sea level using slanted muon detectors that form dense tidal monitor networks<sup>120</sup>. In countries with these conditions, spatiotemporally dense tidal measurements are important to accurately forecast storm surges<sup>121</sup>. The dense tidal measurements enable more accurate forecasts by assimilating observation data. As muography detectors have no direct contact with water in these situations, maintenance costs are lower. Muography detectors have no mechanically moving components, which means malfunctions are less likely than legacy tide gauge stations. As a result, it is easier to achieve long, stable operating conditions<sup>121</sup>.

Near-horizontal muons that travel through the troposphere arrive at a ground-based muography detector after passing through hundreds of kilometres of atmosphere. Atmospheric conditions may include phenomena such as a tropical cyclone or a mesoscale convective system. Consequently, the internal structure of a cyclone and its movement can be measured. For instance, a muographically imaged density profile of a tropic cyclone projected a low-density region corresponding to the warm core<sup>117</sup>. As the magnitude of the vertical density difference inside the cyclone indicates the magnitude of the buoyancy, the vertical density profile taken during a storm can estimate the cyclone's strength. Despite advances in storm track predictions, storm intensity forecasts have not advanced comparably. Muography can improve prediction methodologies and alarm systems. This is because the storm track mostly depends on large-scale atmospheric conditions, which are imaged with satellites, whereas storm intensity relates to the internal dynamics of the cyclone.

In the tropics, atmospheric systems are mainly sustained by latent heat released through cumulus convection. For tropical cyclones in the North Indian Ocean, it is important to discover which mechanism controls the convective processes: conditional instability of the second kind, wind-induced surface heat exchange or something else. An investigation<sup>122</sup> explored the interaction between moist convection and atmospheric circulation in tropical storm systems. Unlike in middle

and high latitudes, convective mechanisms in the tropics vary from season to season and from region to region. As a result, it is essential for the exact mechanism of each storm to be identified. This lack of understanding can be overcome with muographic imagery. For example, a suite of muographic detectors on a coastline where a tropical cyclone makes landfall could probe the cyclone's vertical structure, including its vertical velocity field, and cloud distribution. This could help provide storm intensity data as a series of muographic images.

**Planetary sciences.** In outer space, resource exploration and volcano monitoring can help secure assets and improve safety for the possible future development of extra-terrestrial human or robotic settlements. Although the Moon and Mars<sup>123</sup> present environmental challenges, muography may be applicable on these planetary bodies<sup>124</sup>. Muography teams are planning a series of experiments, starting from simulations on Earth, to test muography in lunar and Martian environments. The muon flux on Mars was estimated<sup>125</sup>. It was also shown<sup>126</sup> that horizontal directions yield more high-energy muons than directions close to the zenith because the horizontally integrated density of the Martian atmosphere is  $\sim 100 \text{ g cm}^{-2}$ . This is opposite to the situation on Earth and equivalent to the depth of the terrestrial atmosphere where the muon flux reaches a maximum. A series of experiments is planned in the Atacama Desert, Chile, which offers an analogous site to physically simulate the logistics of operating muon detectors in a rover on Mars<sup>127</sup>.

## Positioning, navigation and timing

Muometric PNT can potentially be used in many applications, similar to GPS-based PNT, in key sectors of the economy and public security. Muometric techniques offer precise PNT in GPS-denied environments.

**Positioning and navigation.** Positioning, navigation and monitoring in indoor, underground and underwater environments have been modelled and tested. A major application of wired muometric positioning is to monitor three-dimensional tectonic or magmatic-driven seafloor motion with a muPS buoy. This type of monitoring is not possible with conventional techniques. The muPS buoy equips a reference detector and a GPS antenna on the floating section, with the receiver detector at the anchor section. The reference detector is wired to the receiver detector. The position of the receiver detector is determined by the slewing motion of the floating section of the buoy. As an example, to estimate the detector size and measurement time required to obtain useful muPS data from the seafloor, a numerical model<sup>12</sup> looked at three cases: seafloor deformation caused by the Campi Flegrei volcanic activities<sup>128</sup>, Axial Seamount<sup>129</sup> and plate tectonics<sup>130</sup>. Their deformation rates and depths are, respectively, 3 cm per 100 days at  $\sim 100 \text{ m}$ , 2 m per 10 years at  $\sim 1,500 \text{ m}$  and 6 cm per year at  $\sim 2,000 \text{ m}$ . By assuming these experimental configurations, the following measurements conditions were proposed: Campi Flegrei volcanic activities, 1 m<sup>2</sup> detectors attain 2–4 cm accuracy within 100 days; Axial Seamount, 4 m<sup>2</sup> detectors attain 10 cm accuracy within 100 days; and plate tectonics, 20 m<sup>2</sup> detectors attain 5 cm accuracy within 1 year.



An important application of muometric wireless navigation system (MuWNS) is indoor and underground navigation in environments where GPS is unavailable. Indoor navigation has far-reaching application possibilities, including improved automation within homes, hospitals, offices, factories and mines<sup>131–140</sup>. In MuWNS, the clock of the reference detector could be steered by GPS (Fig. 4a), whereas the muon's arrival time at the receiver detector is measured with an independent, high-precision local clock<sup>3</sup>. An investigation<sup>4</sup> of muometric navigation in the basement floor of a building with volume  $200 \times 100 \times 30 \text{ m}^3$  achieved the navigation accuracies summarized in Table 1. Accuracy problems arose from relatively large temporal fluctuations (up to ~50 ns) of the local clocks in the receiver detector. For further improvements, a practical implementation of a chip-scale atomic clock (CSAC) will be needed. MuWNS-V (MuWNS with the vector technique) is another type of wireless navigation system that uses vector muPS<sup>61</sup>. A demonstration at the UTokyo–Wigner Joint Laboratory in Budapest yielded a positioning accuracy of 3.9 cm (standard deviation) within a navigation range of a few metres<sup>141</sup>.

New technologies have been proposed for underground mine positioning and navigation<sup>142</sup>. muPS has the potential to improve open pit activities and management, for example in machine control, collision avoidance, fleet management, surveying and drilling. This could be arranged by including a series of muPS-reference stations in fixed positions near the target open pit and muPS receivers in the vehicles. As mining projects advance deeper underground, risks for fracturing and deformation of the space within the mine become greater due to increased rock pressure. One solution is to automate production by using autonomous machines and robots that could be remotely navigated by MuWNS or wired muPS.

**Time metrology.** Time synchronization techniques are essential for time metrology and are increasingly applied to fundamental science and commercial sectors. In time metrology, time synchronization techniques are used to compute International Atomic Time (TAI) and UTC timescales, as well as for the remote comparison of national realizations of UTC, namely UTC(*k*)<sup>143</sup>. Timing is also crucial in fundamental physics experiments to increase the accuracy of event timestamps and infer the

characteristics of observed phenomena<sup>144</sup>. In the commercial sector, timing is required to synchronize mobile communication systems, digital radio or television broadcasts and smart grids, and for accurate and precise timestamps of financial transactions<sup>145</sup>. Time synchronization is typically achieved by local oscillators – either high-quality quartz or atomic oscillators – with information protocols shared via the Internet or dedicated optical fibres, such as Network Time Protocol (NTP)/Precision Time Protocol (PTP)<sup>146,147</sup> or White Rabbit. Alternatively, satellite techniques can be used<sup>148,149</sup>, which have different performance, functional characteristics, limits, reference markets and users. A back-up or alternative time synchronization technique is necessary to increase timing robustness and resilience for critical infrastructure. CTS enables cheap, long-term wireless synchronization of local clocks in the EAS shower disc, without requiring critical timing information traffic between each CTS sensor. This makes it resistant to jamming and spoofing. An on-site CTS evaluation showed good time synchronization performance spanning 20 min with 30–35 ns (standard deviation (s.d.),  $1\sigma$ ) granularity over nodal distances of 50–60 m (ref. 6). Recently, these operation time and nodal distance limitations have been extended to a 4,200-min span over 180 m while maintaining sub-microsecond granularity (148.8 ns s.d.,  $1\sigma$ ). CTS now can offer wireless time synchronization service to large clusters of financial firms in large cities such as London, New York and Tokyo. Longer-haul time synchronization can be achieved using a daisy chain configuration of CTS sensors, with performance degradation proportional to the square root of the number of nodes.

**Wireless sensor networks and structural health monitoring.** Optimal operation of wireless sensor networks requires nodal time synchronization. High accuracy (<1 μs) is needed for sound velocity measurements<sup>150</sup> and a beamforming array<sup>151</sup>. In GPS-denied environments, each node must operate with a local clock. However, local clocks tend to drift and should be frequently adjusted. In principle, sub-nanosecond time synchronization is attainable in GPS-denied environments with CTC<sup>7</sup>.

CTC can recalibrate clocks in the radiofrequency-shielded box to the same accuracy, making it possible to resynchronize sensor nodes in environments where other radiofrequency devices perform poorly. This feature enhances the flexibility of wireless sensor networks for structural health monitoring<sup>152</sup>. Although there are technical limitations, such as the need for a particle detector, the CTC approach has fewer limits than active radiofrequency-based resynchronization schemes. This enables structural health monitoring of supersonic aircrafts, bridges, wind turbines and structures with sensor nodes that can withstand harsh environments and weather conditions.

## Cryptography

**Near-field wireless security.** Wireless power transfer and building automation systems require near-field communication<sup>8</sup>. However, the security of short-range wireless communications, such as Bluetooth, is insufficient for sensitive information transfer<sup>153–155</sup>. COSMOCAT can enhance the security in wireless power transfer<sup>8</sup> (Fig. 6a), wireless communications<sup>9</sup> (Fig. 6b) and building automation systems<sup>8</sup> (Fig. 6c). As the energy of cosmic-ray muons is high, they are not strongly influenced by the magnetic field generated by the transmitter coil used for wireless power transfer.

**Cloud-based authentication systems and secured communications.** COSMOCAT can generate a data storage system similar to cloud storage, but with resistance to hacking, theft and interference. Security

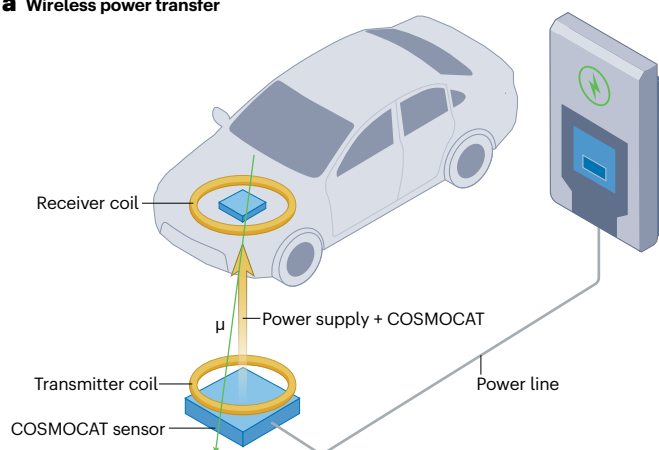
**Table 1 | Comparison of currently achieved MuWNS positioning accuracy and single-point GNSS/GPS positioning in urban areas reported in prior works**

Technique	1s.d. error (m)	Maximum (m)	Ref.
<b>MuWNS-V</b>			
Horizontal (Budapest)	0.039	0.3–0.8	141
<b>MuWNS</b>			
Horizontal (Tokyo)	2.3–14.07	6.0–24.21	4
Vertical (Tokyo)	6.6–9.62	8.0–15.0	4
<b>GPS/GNSS</b>			
Horizontal (Tokyo)	16.1–47.9	102.5–290.7	168
Vertical (Tokyo)	24.8–115.4	167.8–409.7	168
Horizontal (Calgary)	9.4	54.8–97.0	169
Vertical (Calgary)	7.5–15.1	41.1–204.7	169

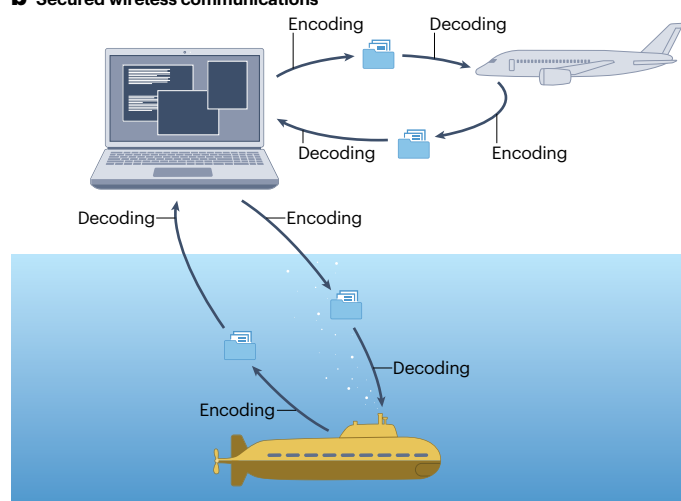
GNSS, global navigation satellite system; GPS, global positioning system; MuWNS, muometric wireless navigation system; MuWNS-V, MuWNS with the vector technique; s.d., standard deviation.



## a Wireless power transfer



## b Secured wireless communications



## c Building automation system

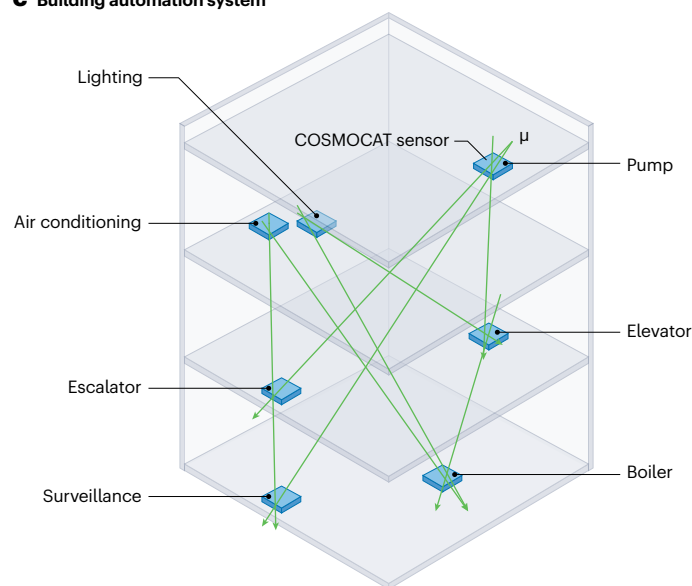


**Fig. 6 | Applications of muometric cryptography.** a–c, Applications for wireless power transfer (panel a), secured unmanned aerial vehicle/autonomous underwater vehicle communications (panel b) and the building automation system (panel c). Green arrows in panels a and c indicate cosmic-ray muons. Blue square-shaped plates indicate cosmic coding and transfer (COSMOCAT) sensors. Parts a and c adapted from ref. 8, CC BY 4.0. Part b adapted from ref. 9, Springer Nature Limited.

assurance for cryptographic keys stored in the cloud is needed<sup>156–158</sup>. If storage is physically accessible, it can be stolen or vandalized. Quantum key distribution (QKD) enables private keys to be shared. QKD can protect data on communication lines, but cannot protect data in storage<sup>159</sup>. COSMOCATS was proposed<sup>9</sup> for electronic money transactions, e-commerce banking applications, issuance of cryptocurrency and secured wireless communications (Fig. 6b). COSMOCAT generates an identical pair of encryption keys without physical key exchange. The COSMOCATS–QKD joint system may offer highly secured key distribution and upgraded security for authentication and data storage<sup>9</sup>.

## Reproducibility and data deposition

Muographic measurements and observations have been conducted in Europe, Asia, the Americas and Africa using the same source: cosmic-ray muons. Measurements and observations can be performed and reproduced globally, regardless of location. Muographic detectors are reproducible as they are built from commercially available components, which have been widely tested and used. Unlike other measurements, muographic data include the exact number of muon events. This makes error analysis simpler. Typically, muographic data are stored with access policies dependent on the group and sites. Data sets are available from global muography groups on request. Some muographic data sets are published in real time. Event by event data are available at the virtual laboratory platform established for the Tokyo Bay seafloor HKMSDD.

## Limitations and optimizations

Although muographic techniques still need to be fully standardized, their potential has been demonstrated. Future challenges may arise from hardware equipment, data analysis software, fieldwork or other factors.

## Hardware

**Cost.** Muographic equipment is usually designed and developed by a professional team with members from several interdisciplinary fields, such as particle and nuclear physics, radiation detection, electronics, machinery and numerical analysis. Currently, particle detection-sensitive materials are rare and expensive due to low industry demand. In addition, some muography hardware systems have many electronic channels, each with several functions. These can be expensive if the system is not designed to be highly integrated. Without mass production, the hardware cost will stay high compared with contemporary instruments used in other disciplines.

**Complexity and expertise.** Hardware used in applied nuclear science is highly specialized. Applying this hardware in field conditions requires engineering and technical professionals. Even with dedicated training, the learning curve for a non-professional may be steeper than for conventional tools in other disciplines. [Introductory videos](#) are sometimes useful for beginners to understand the concept and the principle.

## Glossary

### Cosmic time calibration

(CTC). A decametric-scale wireless clock network resynchronization scheme with approximately nanosecond precision. Cosmic-ray muons are used instead of radiofrequency signals.

### Cosmic time synchronization

(CTS). A hectometric to kilometric-scale wireless clock network resynchronization scheme with precision of 10–100 ns. Extended air shower (EAS) particles are used instead of radiofrequency signals.

### Secondary particles

Secondary cosmic rays generated by interaction between primary cosmic rays and atmospheric nuclei, including various kinds of particles such as mesons, muons and neutrinos.

### True random numbers

(TRNs). Random numbers that are not affected by external factors, intentions, signs or biases. It is impossible to predict what number will come next, even if the generation mechanism is known.

**Portability and all-weather suitability.** For muographic imagery, on-field scenarios are often rugged and isolated from social infrastructure, with some survey sites not easily accessible. Accordingly, features such as portability, robustness, ease of deployment and strength to withstand harsh weather or environmental conditions are in demand for field-qualified muographic hardware.

### Data analysis software and frameworks

Several tools and frameworks are available in the muography community, such as particle transportation frameworks using Monte Carlo techniques<sup>50,160</sup>, the muon surviving rate calculation tool<sup>161</sup>, cosmic-ray flux generators<sup>48</sup>, forward simulation and the three-dimensional numerical inversion tool<sup>162,163</sup>. However, as muography evolves, a universal system with a standardized tool kit is needed. Professional analysis expertise is required for almost all applications. Muographic analysis usually involves processing, data preparation and modelling, which should be performed by well-trained professionals. Experts in the problems under study are also needed, such as geologists, engineers or archaeologists.

### Fieldwork

**Survey duration.** The need for long-duration surveys is an issue frequently brought up by muography users and researchers. In some scenarios, several weeks or months may be required to obtain sufficient data statistics, which may not be suitable for all applications. Temporary changes or dynamic movements in the targeted area may be challenging to capture. As the cosmic-ray muon flux is essentially fixed, the detection system should have a large detection area and high detection efficiency to reduce imaging times.

**Feasibility studies before surveying.** Not all structures are suitable for muographic imaging. As a result, feasibility studies are crucial. A feasibility study must be performed prior to an on-field scan to ensure the task can be successfully performed with the requested resolution and within the survey time duration parameters.

### Outlook

Currently, detector costs per unit area are too expensive for widespread and large-scale implementation. Therefore, a critical development is to

reduce detector costs. For example, triangular extrusions with scintillating pellets lowers the cost of building online detectors<sup>164</sup>. The project exploring the Great Pyramid aims to produce a 2,000 m<sup>2</sup> detector at a reasonable price<sup>22</sup>. In this section, possible future instrumentation for each muographic theme is discussed.

### Future instrumentation

**Imaging.** There is a demand for muography to image high-temperature objects (>500 °C) under high-pressure conditions, for example near or within a geothermal reservoir, a magma chamber or Venusian atmosphere. Scintillation detectors are not an option, as plastic scintillators melt under these conditions. To construct a robust muography observation system capable of operating under extreme environmental conditions, stainless steel welded proportional counters could be a good option. As the structure of each stainless steel welded proportional counter is simple, a gas-filled metallic tube with a wire anode, the detector is likely to survive the physically demanding exposure to high temperatures, shocks and vibrations. Additionally, the stainless steel welded proportional counter was designed for protection against high pressure. The SUS-304-type stainless steel contains nickel and molybdenum for durability against typical acids. At high temperatures the counter operation is influenced by thermal electrons emitted from the cathode material. The maximum operating temperature of a proportional counter was reported<sup>165</sup> as ~800 °C when an iron foil was mounted as a cathode.

In the future, machine learning-assisted muon spectra analysers<sup>166</sup> may enable large-sized meteorite samples to be inspected, such as Gibeon, by selecting the momentum of the incident muons. By studying meteorite pores, the size of the asteroid they originated from can be determined.

**Navigation.** Wireless navigation precision depends on how accurately the muon's TOF can be determined wirelessly. Improvements in wireless logical processing systems incorporating a CSAC are required. For example, the currently available **rubidium CSAC (SPARKX SPX 14830)** (1.5 µs per day) has a one order of magnitude improvement in drift rate compared with **oven-controlled crystal oscillators** (1.5 µs over 4 h), leading to one order of magnitude better accuracy than the current MuWNS presented in Table 1. It has a size of 18.3 × 50.8 × 50.8 mm<sup>3</sup> and weight 55 g, making it easy to incorporate into a MuWNS. The price is relatively high (US\$2,000 per chip), but costs are expected to decrease with the introduction of 5G networks.

**Timing.** CTS offers high-level, continuous performance for a potential self-adjusting clock system, for example, as a GPS back-up. CTS could be used to disseminate reference atomic timescales to final users in a city, with improved robustness and reliability. It is complementary to other time synchronization techniques, is suitable for critical applications in optical fibres<sup>167</sup> and could be retrofitted for compatibility with existing time synchronization techniques and time protocols, for instance Inter-Range Instrumentation Group B (IRIG-B), NTP and PTP. CTS could be used by individuals who require precise and accurate timestamps that are traceable to a reference timescale, such as UTC<sup>6</sup>. At present, this is achieved with NTP/PTP or White Rabbit protocols, among others. Another CTS application could be for users requiring 1 PPS and 10 MHz precise and accurate reference signals. For both cases, typical users may come from scientific fields or commercial sectors. These practical applications and implementations of CTS are currently under construction at the **Facility for High Timing Accuracy for Fundamental Physics Experiments of the Italian National Metrological Institute (INRiM)**.

**Cryptography.** Drone development has accelerated, with applications expanding to the Internet of Drones (IoD). The IoD can offer interactive and ubiquitous connectivity between individuals. For example, a drone-based delivery system has been demonstrated in Australia. Although the IoD brings convenience, it can be hazardous if drone communication links are cracked and hijacked. In the future, highly secure drone-based wireless sensor networks will be needed. The travelling speed of cosmic-ray muons is close to the speed of light in a vacuum, much faster than other moving objects on the Earth. As a result, the application range of COSMOCAT can be extended from static targets – building automation systems, wireless power transfer – to moving targets, such as drones. Future developments of COSMOCATS could be used for secured IoD systems.

In conclusion, muography is more than a way to measure structures, time, movement and various phenomena. There is also more to being a muographer than being proficient in the various applications and techniques of muography. Providing practical measurements to solve real-world problems for researchers, industry and the public is only one goal of this academic field. By uncovering new observations about the Earth and by improving data security, timed communication and navigation of autonomous or human subjects, unique insights and shared data sets collected from several locations can be compared, enabling patterns to be recognized. The field of muography aims to examine and define the role of the muon in society. In this Primer, a broad overview of muography has been provided, including how it has been applied to different systems around the world.

Published online: 23 November 2023

## References

1. Tanaka, H. K. M. Particle geophysics. *Ann. Rev. Earth Planet. Sci.* **42**, 535–549 (2014).
2. Tanaka, H. K. M. Muometric positioning system ( $\mu$ PS) with cosmic muons as a new underwater and underground positioning technique. *Sci. Rep.* **10**, 18896 (2020).  
**To our knowledge, this work is the first proposal of  $\mu$ PS and demonstration of the laboratory-scale  $\mu$ PS.**
3. Tanaka, H. K. M. Wireless muometric navigation system. *Sci. Rep.* **12**, 10114 (2022).
4. Tanaka, H. K. M. et al. First navigation with wireless muometric navigation system ( $\mu$ WNS) in indoor and underground environments. *iScience* **26**, 107000 (2023).  
**To our knowledge, this work is the first demonstration of wireless navigation based on  $\mu$ PS in the GPS-denied environment.**
5. Tanaka, H. K. M. Cosmic time synchronizer (CTS) for wireless and precise time synchronization using extended air showers. *Sci. Rep.* **12**, 7078 (2022).  
**To our knowledge, this work is the first proposal of <100 ns time synchronization with the EAS.**
6. Tanaka, H. K. M., Cerretto, G. & Gnesi, I. Cosmic time synchronization (CTS): first experimental results for a wireless, precise, and perpetual time synchronization system with extended air shower particles. *iScience* **26**, 106595 (2023).  
**To our knowledge, this work is the first successful demonstration of <100 ns time synchronization with the EAS.**
7. Tanaka, H. K. M. Cosmic time calibrator for wireless sensor network. *Sci. Rep.* **13**, 5951 (2023).
8. Tanaka, H. K. M. Cosmic coding and transfer for ultra high security near-field communications. *iScience* **26**, 105897 (2023).  
**To our knowledge, this work is the first proposal and demonstration of encryption key generation and transfer with cosmic-ray muons.**
9. Tanaka, H. K. M. Cosmic coding and transfer storage (COSMOCATS) for invincible key storage. *Sci. Rep.* **13**, 8746 (2023).
10. Particle Data Group. Review of particle physics. *Prog. Theor. Exp. Phys.* **2022**, 083C01 (2022).
11. Oláh, L., Tanaka, H. K. M. & Varga, D. Muography: exploring earth's subsurface with elementary particles. *Geophys. Monogr.* **270**, 1–306 (2022).
12. Giammanco, A. et al. Muon imaging present status and emerging applications. *International Atomic Energy Agency* <https://www.iaea.org/publications/15182/muon-imaging> (2022).
13. Scampoli, P. & Ariga, A. *Cosmic Ray Muography* (eds Scampoli, P. & Ariga, A.) 1–308 (World Scientific, 2023).
14. Engel, R., Gaisser, T. K. & Stanev, T. The flux of atmospheric muons. *Proc. ICRC* **2001**, 1029–1032 (2001).
15. Conversi, M. Experiments on cosmic-ray mesons and protons at several altitudes and latitudes. *Phys. Rev.* **79**, 749 (1950).
16. Allkofer, O. C., Clausen, K. & Dau, W. D. The low-momentum muon spectrum near the equator. *Lett. Nuovo Cim.* **12**, 107–110 (1975).
17. Groom, D. E. et al. Muon stopping-power and range tables: 10 MeV–100 TeV. *At. Data Nucl. Data Tables* **78**, 183–356 (2001).
18. Tanaka, H. K. M. et al. Development of the cosmic-ray muon detection system for probing internal-structure of a volcano. *Hyper. Inter.* **138**, 521–526 (2001).
19. Taira, H. & Tanaka, H. K. M. A potential space- and power-effective muon sensor module for imaging a volcano. *Earth Planet. Space* **62**, 179–186 (2010).
20. Anastasio, A. et al. The MU-RAY detector for muon radiography of volcanoes. *Nucl. Instr. Meth. Phys. Res. A* **732**, 423–426 (2013).
21. Lo Presti, D. et al. Development of a scintillation-fiber detector for real-time particle tracking. *J. Instr.* **8**, P04015 (2013).
22. Bross A. Tomographic muon imaging of the great pyramid of giza. *J. Adv. Instr. Sci.* **2022**, 1–9 (2022).
23. Marteau, J. et al. Muon tomography applied to geosciences and volcanology. *Nucl. Instr. Meth. Phys. Res. A* **695**, 23–28 (2012).
24. D'Errico, M. et al. The muraves experiment: a study of the vesuvius great cone with muon radiography. *J. Adv. Instr. Sci.* **2022**, 273 (2022).
25. Charpak, G., Bouclier, R., Bressani, T., Favier, J. & Zupancic, C. The use of multiwire proportional counters to select and localize charged particles. *Nucl. Instr. Meth. Phys. Res. A* **62**, 262–268 (1968).
26. Blum, W. & Rolandi, L. *Particle Detection with Drift Chambers* (Springer-Verlag, 1993).
27. Varga, D., Nyitrai, G., Hamar, G. & Oláh, L. High efficiency gaseous tracking detector for cosmic muon radiography. *Adv. High. Energy Phys.* **2016**, 1962317 (2016).
28. Oláh, L., Tanaka, H. K. M., Ohminato, T. & Varga, D. High-definition and low-noise muography of the Sakurajima volcano with gaseous tracking detectors. *Sci. Rep.* **8**, 3207 (2018).
29. Bouteille, S. et al. A micromegas-based telescope for muon tomography: the WatTo experiment. *Nucl. Instr. Meth. Phys. Res. A* **834**, 223–228 (2016).
30. Nyitrai, G., Hamar, G. & Varga, D. Toward low gas consumption of muographic tracking detectors in field applications. *J. Appl. Phys.* **129**, 244901 (2021).
31. Gera, Á., Nyitrai, G., Surányi, G., Hamar, G. & Varga, D. Gaseous detectors for field applications: quality control, thermal and mechanical stability. *Instruments* **6**, 74 (2022).
32. Lázaro Roche, I. A compact muon tracker for dynamic tomography of density based on a thin time projection chamber with micromegas readout. *Particles* **4**, 333–342 (2021).
33. Aharonian, F. A., Hofmann, W., Konopelko, A. K. & Völck, H. J. The potential of ground based arrays of imaging atmospheric Cherenkov telescopes. I. Determination of shower parameters. *Astrop. Phys.* **6**, 343–368 (1997).
34. Compagnino, A. A. et al. Evaluating the night sky background directly from the signal images detected by the ASTRI telescopes. *Exp. Astron.* **53**, 1017–1035 (2022).
35. Barkas, W. H. *Nuclear Research Emulsion* (Academic, 1973).
36. Niwa, K. et al. Auto scanning and measuring system for the emulsion chamber. *Proc. Int. Cosmic Ray Symp. High. Energy Phenomena, Cosmic Ray Lab. Univ. Tokyo* **1974**, 149 (1974).
37. Aoki, S. et al. Fully automated emulsion analysis system. *Nucl. Instrum. Meth. B* **51**, 466 (1990).
38. Fukuda, T. et al. Automatic scanning of nuclear emulsions with wide-angle acceptance for nuclear fragment detection. *J. Instr.* **8**, P01023 (2013).
39. Armenise, N. et al. High-speed particle tracking in nuclear emulsion by last-generation automatic microscopes. *Nucl. Instr. Meth Phys. Res. A* **551**, 261–270 (2005).
40. Arrabito, L. et al. Hardware performance of a scanning system for high speed analysis of nuclear emulsions. *Nucl. Instr. Meth Phys. Res. A* **568**, 578–587 (2006).
41. Bozza C. Final version of SySal2000. *Zenodo* <https://doi.org/10.5281/zenodo.4271673> (2000).
42. Bozza, C. et al. An integrated system for large scale scanning of nuclear emulsions. *Nucl. Instr. Meth Phys. Res. A* **703**, 204–212 (2013).
43. Morishima, K. & Nakano, T. Development of a new automatic nuclear emulsion scanning system, S-UTS, with continuous 3D tomographic image read-out. *J. Inst.* **5**, P04011 (2010).
44. Bozza C. et al. GPU-based quasi-real-time track recognition in imaging devices: from raw data to particle tracks. *DESY Library* <https://doi.org/10.3204/DESY-PROC-2014-05/2> (2014).
45. Alexandrov, A. A new generation scanning system for the high-speed analysis of nuclear emulsions. *J. Inst.* **11**, P06002 (2016).
46. Yoshimoto, M. et al. Hyper-track selector nuclear emulsion readout system aimed at scanning an area of one thousand square meters. *Prog. Theor. Exp. Phys.* **10**, 103H01 (2017).
47. D. Heck et al. CORSIKA: a Monte Carlo code to simulate extensive air showers. *Forschungszentrum Karlsruhe GmbH* <https://publikationen.bibliothek.kit.edu/270043064/3813660> (1998).
48. Hagmann C. et al. Cosmic-ray shower generator (CRY) for Monte Carlo transport codes. *IEEE Xplore* <https://ieeexplore.ieee.org/document/4437209> (2007).
49. Cillis, A. N. & Sciutto, S. J. Extended air showers and muon interactions. *Phys. Rev. D* **64**, 013010 (2001).
50. Agostinelli, S. et al. GEANT4 — a simulation toolkit. *Nucl. Inst. Methods A* **506**, 250–303 (2003).
51. Niess, V. et al. Backward Monte-Carlo applied to muon transport. *Comput. Phys. Comm.* **229**, 54 (2018).
52. Baccani, G. et al. The MIMA project. Design, construction and performances of a compact hodoscope for muon radiography applications in the context of archaeology and geophysical prospectives. *J. Instrum.* **13**, P11001 (2018).



53. Lázaro Roche, I. et al. MUon survey tomography based on micromegas detectors for unreachable sites technology (MUST2): overview and outlook. *J. Phys.* **1498**, 012048 (2020).
54. Chaiwongkhot, K. et al. Development of a portable muography detector for infrastructure degradation investigation. *IEEE Trans. Nucl. Sci.* **65**, 2316 (2018).
55. Hamar, G. et al. Underground muography with portable gaseous detectors. *J. Phys.* **2374**, 012186 (2022).
56. Gamage, R. M. I. D. et al. A portable muon telescope for multidisciplinary applications. *J. Instr.* **17**, C01051 (2022).
57. Yifan, Z. et al. Discrimination of drugs and explosives in cargo inspections by applying machine learning in muon tomography. *High. Power Laser Part. Beams* **30**, 086002 (2018).
58. Mahon, D. et al. First-of-a-kind muography for nuclear waste characterization. *Philos. Trans. R. Soc. London, Ser. A* **377**, 2137 20180048 (2019).
59. Barnes, S. et al. Cosmic-ray tomography for border security. *Instruments* **7**, 13 (2023).
60. Bikit, I. et al. Novel approach to imaging by cosmic-ray muons. *EPL* **113**, 58001 (2016).
61. Tanaka, H. K. M. Muometric positioning system (muPS) utilizing direction vectors of cosmic-ray muons for wireless indoor navigation at a centimeter-level accuracy. *Sci. Rep.* **13**, 15272 (2023).
62. Ahlen, S. P. et al. Arrival time distributions of very high energy cosmic ray muons in MACRO. *Nucl. Phys. B* **370**, 432–444 (1992).
63. Kim, K. et al. Massively parallel ultrafast random bit generation with a chip-scale laser. *Science* **371**, 948–952 (2021).
64. Rivest, R. L. et al. A method for obtaining digital signatures and public-key cryptosystems. *Commun. ACM* **21**, 120–126 (1978).
65. Gisin, N. et al. Quantum cryptography. *Rev. Mod. Phys.* **74**, 145–195 (2002).
66. Schouten, D. & Ledru, P. Muon tomography applied to a dense uranium deposit at the McArthur River mine. *J. Geophys. Res. Solid. Earth* **123**, 8637–8652 (2018).
67. George, E. P. Cosmic rays measure overburden of tunnel. *Commonw. Eng.* **1955**, 455–457 (1955).
68. Nishiyama, R. et al. First measurement of ice–bedrock interface of alpine glaciers by cosmic muon radiography. *Geophys. Res. Lett.* **44**, 6244–6251 (2017).
69. Nagamine, K. et al. Probing the inner structure of blast furnaces by cosmic-ray muon radiography. *Proc. Jpn. Acad. Ser. B* **81**, 275–260 (2005).
70. Procureur, S. et al. 3D imaging of a nuclear reactor using muography measurements. *Sci. Adv.* **9**, eabq8431 (2023).
71. Morishima, K. Visualization of molten debris of Fukushima Daiichi nuclear power plant by cosmic ray muon radiography. *Oyo Butsuri* **86**, 950–955 (2017).
72. Thompson, L. F. et al. Muon tomography for railway tunnel imaging. *Phys. Rev. Res.* **2**, 023017 (2020).
73. Oláh, L. et al. The first prototype of an MWPC-based borehole-detector and its application for muography of an underground pillar. *Butsuri-Tansa* **71**, 161–168 (2018).
74. Durham, J. M. et al. Tests of cosmic ray radiography for power industry applications. *AIP Adv.* **5**, 067111 (2015).
75. Morishima, K. et al. Discovery of a big void in Khufu's Pyramid by observation of cosmic-ray muons. *Nature* **552**, 386–390 (2017).  
**This work presents the muographic measurement that has led to discovery of a new chamber inside the Cheops Pyramid. To our knowledge, the first discovery in 189 years.**
76. Procureur, S. et al. Precise characterization of a corridor-shaped structure in Khufu's Pyramid by observation of cosmic-ray muons. *Nat. Commun.* **14**, 1144 (2023).
77. Nagamine, K. et al. Method of probing inner-structure of geophysical substance with the horizontal cosmic-ray muons and possible application to volcanic eruption. *Nucl. Instr. Meth. A* **356**, 585–595 (1995).
78. Caffau, E. et al. Underground cosmic-ray measurement for morphological reconstruction of the “Grotta Gigante” natural cave. *Nucl. Instr. Meth. A* **385**, 480–488 (1997).
79. Tanaka, H. K. M. et al. High resolution imaging in the inhomogeneous crust with cosmic-ray muon radiography: the density structure below the volcanic crater floor of Mt. Asama, Japan. *Earth Planet. Sci. Lett.* **263**, 104–113 (2007).  
**To our knowledge, this work presents the first successful muographic experiments ever to find an unknown structure inside a gigantic object (a volcano).**
80. Kusagaya, T. & Tanaka, H. K. M. Muographic imaging with a multi-layered telescope and its application to the study of the subsurface structure of a volcano. *Proc. Jpn. Acad. Ser. B* **91**, 501–510 (2015).
81. Tanaka, H. K. M., Uchida, T., Tanaka, M., Shinohara, H. & Taira, H. Cosmic-ray muon imaging of magma in conduit: degassing process of Satsuma-Iwojima Volcano, Japan. *Geophys. Res. Lett.* **36**, L01304 (2009).
82. Tanaka, H. K. M. et al. Three-dimensional computational axial tomography scan of a volcano with cosmic ray muon radiography. *J. Geophys. Res.* **115**, B12332 (2010).
83. Tanaka, H. Muographic mapping of the subsurface density structures in Miura, Boso and Izu peninsulas, Japan. *Sci. Rep.* **5**, 8305 (2015).
84. Miyamoto, S. et al. A muographic study of a scoria cone from 11 directions using nuclear emulsion cloud chambers. *Geosci. Instrum. Method. Data Syst.* **11**, 127–147 (2022).
85. Tanaka, H. K. M. Instant snapshot of the internal structure of Unzen lava dome, Japan with airborne muography. *Sci. Rep.* **6**, 39741 (2016).
86. Kusagaya, T. & Tanaka, H. K. M. Development of the very long-range cosmic-ray muon radiographic imaging technique to explore the internal structure of an erupting volcano, Shinmoe-dake, Japan. *Geosci. Instrum. Method. Data Syst.* **4**, 215–226 (2015).
87. Oláh, L. & Tanaka, H. K. M. Machine learning with muographic images as input: an application to volcano eruption forecasting. *Geophys. Monogr.* **270**, 43–54 (2022).
88. Oláh, L. et al. Muon imaging of volcanic conduit explains link between eruption frequency and ground deformation. *Geophys. Res. Lett.* **50**, e2022GL101170 (2023).
89. Tanaka, H. K. M. et al. Cosmic-ray muon imaging of magma in a conduit: degassing process of Satsuma-Iwojima volcano, Japan. *Geophys. Res. Lett.* **36**, L01304 (2009).
90. Tanaka, H., Kusagaya, T. & Shinohara, H. Radiographic visualization of magma dynamics in an erupting volcano. *Nat. Commun.* **5**, 3381 (2014).  
**To our knowledge, this work presents the first successful muographic image capturing of ascent and descent of the magma column inside an erupting volcano.**
91. Lesparre, N. et al. Density muon radiography of La Soufrière de Guadeloupe volcano: comparison with geological, electrical resistivity and gravity data. *Geophys. J. Inter.* **190**, 1008–1019 (2012).
92. Ambrosino, F. et al. Joint measurement of the atmospheric muon flux through the Puy de Dôme volcano with plastic scintillators and resistive plate chambers detectors. *J. Geophys. Res.* **120**, 7290–7307 (2015).
93. Lo Presti, D. et al. Muographic monitoring of the volcano-tectonic evolution of Mount Etna. *Sci. Rep.* **10**, 11351 (2020).
94. Tioukov, V. et al. First muography of Stromboli volcano. *Sci. Rep.* **9**, 6695 (2019).
95. Jourde, K. et al. Muon dynamic radiography of density changes induced by hydrothermal activity at the La Soufrière de Guadeloupe volcano. *Sci. Rep.* **6**, 33406 (2016).
96. Oláh, L., Tanaka, H. K. M. & Hamar, G. Muographic monitoring of hydrogeomorphic changes induced by post-eruptive lahars and erosion of Sakurajima volcano. *Sci. Rep.* **11**, 17729 (2021).
97. Okubo, S. & Tanaka, H. K. M. Imaging the density profile of a volcano interior with cosmic-ray muon radiography combined with classical gravimetry. *Meas. Sci. Technol.* **23**, 042001 (2012).
98. Nishiyama, R. et al. Integrated processing of muon radiography and gravity anomaly data toward the realization of high-resolution 3-D density structural analysis of volcanoes: case study of Showa-Shinzan lava dome, Usu, Japan. *J. Geophys. Res.* **119**, 699–710 (2014).
99. Rosas-Carbajal, M. et al. Three-dimensional density structure of La Soufrière de Guadeloupe lava dome from simultaneous muon radiographies and gravity data. *Geophys. Res. Lett.* **44**, 6743–6751 (2017).
100. Le Gonidec, Y. et al. Abrupt changes of hydrothermal activity in a lava dome detected by combined seismic and muon monitoring. *Sci. Rep.* **9**, 3079 (2019).
101. Leone, G. et al. Muography as a new complementary tool in monitoring volcanic hazard: implications for early warning systems. *Proc. R. Soc. A* **477**, 20210320 (2021).
102. Shinohara, H. & Tanaka, H. K. M. Conduit magma convection of a rhyolitic magma: constraints from cosmic-ray muon radiography of Iwodake, Satsuma-Iwojima volcano, Japan. *Earth Planet. Sci. Lett.* **349–350**, 87–97 (2012).
103. Alvarez, L. W. et al. Search for hidden chambers in the pyramid. *Science* **167**, 832–739 (1970).
104. Tanaka, H. K. M., Sumiya, K. & Oláh, L. Muography as a new tool to study the historic earthquakes recorded in ancient burial mounds. *Geosci. Instrum. Method. Data Syst.* **9**, 357–364 (2020).
105. Liu, G. et al. High-precision muography in archaeogeophysics: a case study on Xi'an defensive walls. *J. Appl. Phys.* **133**, 014901 (2023).
106. Hanazato, T. et al. Muon radiography monitoring for structural survey of the Prambanan World Heritage Temple. *Japan Geoscience Union* <https://www2.jpgu.org/meeting/2014/session/PDF/U-02/U02-07.pdf> (2014).
107. Saracino, G. et al. Imaging of underground cavities with cosmic-ray muons from observations at Mt. Echia (Naples). *Sci. Rep.* **7**, 1181 (2017).
108. Cimmino, L. et al. 3D muography for the search of hidden cavities. *Sci. Rep.* **9**, 2974 (2019).
109. Elkarmoty, M. et al. Localization and shape determination of a hidden corridor in the Great Pyramid of giza using non-destructive testing. *NDT&E Int.* **123**, 102809 (2023).
110. Tanaka, H. K. M. & Ohshiro, M. Muographic data analysis method for medium-sized rock overburden inspections. *Geosci. Instrum. Method. Data Syst.* **5**, 427–435 (2016).
111. Klaus, R. Lifting work and building time at the 4th dynasty pyramids. *Trabajos de. Egipto.* **12**, 85–111 (2021).
112. Tanaka, H. K. M. et al. Cosmic muon imaging of hidden seismic fault zones: rainwater permeation into the mechanical fractured zones in Itoigawa–Shizuoka Tectonic Line, Japan. *Earth Planet. Sci. Lett.* **306**, 156–162 (2011).
113. Lázaro Roche, I. et al. Water resource management: the multi-technique approach of the low background noise underground research laboratory and its muon detection projects. *Geophys. Monogr.* **270**, 137–152 (2022).
114. Holma, M., Zhang, Z.-X., Kuusiniemi, P., Loo, K. & Enqvist, T. Future prospects of muography for geological research and geotechnical and mining engineering. *Geophys. Monogr.* **270**, 199–219 (2022).
115. Zhang, Z.-X., Enqvist, T., Holma, M. & Kuusiniemi, P. Muography and its potential applications to mining and rock engineering. *Rock. Mech. Rock Eng.* **53**, 4893–4907 (2022).
116. Marteau, J. et al. Development of scintillator-based muon detectors for muography. *Geophys. Monogr.* **270**, 237–252 (2022).
117. Tanaka, H. K. M. et al. Atmospheric muography for imaging and monitoring tropic cyclones. *Sci. Rep.* **12**, 16710 (2022).  
**To our knowledge, this work presents the first successful muographic experiments to image the atmosphere (a cyclone).**
118. Tanaka, H. K. M. et al. Periodic sea-level oscillation in Tokyo Bay detected with the Tokyo-Bay seafloor hyper-kilometric submarine deep detector (TS-HKMSSD). *Sci. Rep.* **12**, 6097 (2022).  
**To our knowledge, this work presents the first successful muographic application to the sea and the first detection of tsunami with muography.**



119. Tanaka, H. K. et al. First results of undersea muography with the Tokyo-Bay seafloor hyper-kilometric submarine deep detector. *Sci. Rep.* **11**, 19485 (2021).
120. Tanaka, H. K. M. Muography for a dense tide monitoring network. *Sci. Rep.* **12**, 6725 (2022).
121. Verlaan, M. et al. Operational storm surge forecasting in the Netherlands: developments in the last decade. *Philos. Trans. R. Soc. A* **363**, 1441–1453 (2005).
122. Tomassini, L. The interaction between moist convection and the atmospheric circulation in the tropics. *Bull. Am. Meteorol. Soc.* **101**, E1378–E1396 (2022).
123. Leone, G., Ahrens, C., Calabrese, G., Tanaka, H. K. M. & D'Incecco, P. in *Mars: A Volcanic World* (ed. Leone, G.) 309–323 (Springer International, 2021).
124. Holma, M., Joutsenvaara, J. & Kuusiniemi, P. Astroparticle physics obtaining more attention from a new type of audience. *J. Phys. Conf. Ser.* **2156**, 12178 (2021).
125. Tanaka, H. K. M. Monte-Carlo simulations of atmospheric muon production: implication of the past martian environment. *Icarus* **191**, 603–615 (2007).
126. Kedar, S. et al. Muon radiography for exploration of Mars geology. *Geosci. Instr. Methods Data Syst.* **2**, 157–164 (2013).
127. Azua-Bustos, A., González-Silva, C. & Fairén, A. G. The atacama desert in northern Chile as an analog model of Mars. *Front. Astron. Sp. Sci.* **8**, 242 (2022).
128. Chierici, F. et al. A new method to assess long-term sea-bottom vertical displacement in shallow water using a bottom pressuresensor: application to Campi Flegrei, southern Italy. *J. Geophys. Res.* **121**, 7775–7789 (2016).
129. Chadwick, W. W., Nooner, S. L., Butterfield, D. A. & Lilley, M. D. Seafloor deformation and forecasts of the April 2011 eruption at Axial Seamount. *Nat. Geosc.* **5**, 474–477 (2012).
130. Gagnon, K., Chadwell, C. D. & Norabuena, E. Measuring the onset of locking in the Peru–Chile trench with GPS and acoustic measurements. *Nature* **434**, 205–208 (2005).
131. Kosaka, A. & Kak, A. C. Fast vision-guided mobile robot navigation using model-based reasoning and prediction of uncertainties. *Comput. Vis. Image. Underst.* **56**, 271–329 (1992).
132. Lu, F. & Milios, E. Robot pose estimation in unknown environments by matching 2D range scans. *J. Intell. Robot. Syst.* **18**, 249–275 (1997).
133. Motomura, A. et al. Real-time self-localization method by using measurements of directions of two landmarks and dead reckoning. *J. Robot. Soc. Jpn.* **23**, 39–48 (2005).
134. El-hakim, S. et al. A mobile system for indoors 3-D mapping and positioning. in *3-D Measurement Techniques* [https://www.academia.edu/20708330/A\\_mobile\\_system\\_for\\_indoors\\_3\\_D\\_mapping\\_and\\_positioning](https://www.academia.edu/20708330/A_mobile_system_for_indoors_3_D_mapping_and_positioning) (1997).
135. Sertatil, C. et al. A novel acoustic indoor localization system employing CDMA. *Digit. Sig. Process.* **22**, 506–517 (2012).
136. Hahnel, D. et al. Learning compact 3D models of indoor and outdoor environments with a mobile robot. *Rob. Auton. Syst.* **44**, 15–27 (2003).
137. Kelly, A. in *Proceedings 2001 IEEE/RSJ International Conference on Intelligent Robots and Systems. Expanding the Societal Role of Robotics in the the Next Millennium* (Cat. No. 01CH37180) <https://ieeexplore.ieee.org/document/976357> (IEEE, 2001).
138. Crowley, J. L. in *Proceedings, 1989 International Conference on Robotics and Automation* <https://ieeexplore.ieee.org/document/100156> (IEEE, 1989).
139. Kataria, S. et al. Survey paper on wireless underground positioning system. *Int. J. Comp. Appl.* **130**, 1–4 (2015).
140. Chow, J. F. et al. Toward underground localization: lidar inertial odometry enabled aerial robot navigation. *arXiv* **1910**, 13085v1 (2019).
141. Varga, D. & Tanaka, H. K. M. Developments of a centimeter-level precise muometric wireless navigation system (MuWNS-V) and its first demonstration using directional information from tracking detectors. *arXiv* **2308**, 10108 (2023).
142. Seguel, F. et al. Underground mine positioning: a review. *IEEE Sens. J.* **22**, 4755–4771 (2022).
143. Panfilo, G. & Arias, F. The coordinated universal time. *Metrologia* **56**, 042001 (2019).
144. Cerretto, G. et al. Extensive cosmic showers detection: the importance of timing and the role of GPS in the EEE experiment. *GPS Solut.* **25**, 125 (2021).
145. Directive 2014/65/EU of the European Parliament and of the Council of 15 May 2014 on markets in financial instruments and amending Directive 2002/92/EC and Directive 2011/61/EU (recast) Text with EEA relevance. *EUR-Lex* <https://eur-lex.europa.eu/legal-content/EN/ALL/?uri=CELEX%3A32014L0065> (2014).
146. Smotlacha, V. et al. On calibration of network time services. *Metrologia* **45**, S51 (2008).
147. Mkacher F. & Duda A. in *2019 IEEE International Symposium on Precision Clock Synchronization for Measurement, Control, and Communication (ISPCS)* <https://ieeexplore.ieee.org/document/888664> (IEEE, 2019).
148. Petit, G. & Jiang, Z. GPS all in view time transfer for TAI computation. *Metrologia* **45**, 35 (2008).
149. Jiang, Z. & Petit, G. Combination of TWSTFT and GNSS for accurate UTC time transfer. *Metrologia* **46**, 305 (2009).
150. Merrill, W. et al. Autonomous position location in distributed, embedded, wireless systems. *Sensoria* [https://web.archive.org/web/20200709212914/https://descanso.jpl.nasa.gov/symposia/ieee\\_cas2002/full/merrill.pdf](https://web.archive.org/web/20200709212914/https://descanso.jpl.nasa.gov/symposia/ieee_cas2002/full/merrill.pdf) (2002).
151. Cerpa, A. et al. Habitat monitoring: application driver for wireless communications technology. in *Proc. SIGCOMM LA '01: Workshop on Data communication in Latin America and the Caribbean* <https://doi.org/10.1145/371626.371720> (2001).
152. Sazonov, E. et al. Wireless intelligent sensor and actuator network — a scalable platform for time synchronous applications of structural health monitoring. *Struct. Health Monitor.* **9**, 465–476 (2010).
153. Padgett, J. & Scarfone, K. NIST special publication 800-121 revision 1, guide to Bluetooth security (National Institute of Standards and Technology, 2012).
154. Zhang, Z. et al. Improvement of electromagnetic compatibility of motor drives using hybrid chaotic pulse width modulation. *IEEE Trans. Magn.* **47**, 4018–4021 (2011).
155. Ye, S. & Chau, K. T. Chaoization of DC motors for industrial mixing. *IEEE Trans. Ind. Electron.* **54**, 2024–2032 (2007).
156. Prajapati, P. & Shah, P. A review on secure data deduplication: cloud storage security issue. *J. King Saud. Univ. Comput. Inf. Sci.* **34**, 3996–4007 (2022).
157. National Institute of Standards and Technology. Cryptographic key management issues & challenges in cloud services. *NIST Technical Series Publications* <https://nvlpubs.nist.gov/nistpubs/ir/2013/nist.ir.7956.pdf> (2013).
158. Lin, H.-Y. & Tzeng, W.-G. A secure erasure code-based cloud storage system with secure data forwarding. *IEEE Trans. Parallel Distrib. Syst.* **23**, 995–1003 (2012).
159. National Cyber Security Centre. Quantum security technologies. *National Cyber Security Centre* <https://www.ncsc.gov.uk/whitepaper/quantum-security-technologies> (2016).
160. Battistoni, G. et al. Overview of the FLUKA code. *Ann. Nucl. Energy* **82**, 10–18 (2015).
161. Kudryavtsev, V. A. Muon simulation codes MUSIC and MUSUN for underground physics. *Comput. Phys. Commun.* **180**, 339–346 (2009).
162. Cockett, R. et al. SimPEG: an open source framework for simulation and gradient based parameter estimation in geophysical applications. *Comput. Geosci.* **85**, 142–154 (2015).
163. Rücker, C. et al. An open-source library for modelling and inversion in geophysics. *Comput. Geosci.* **109**, 106–123 (2017).
164. Pla-Dalmau, A. et al. Low-cost extruded plastic scintillator. *Nucl. Instr. Meth. Phys. Res. A* **466**, 482–491 (2001).
165. Isozumi, Y. et al. High-temperature proportional counter and its application to resonance-electron Mössbauer spectroscopy. *Sci. Instrum.* **52**, 413 (1981).
166. Oláh, L. et al. Development of machine learning-assisted spectra analyzer for the newcut muon spectrometer. *J. Adv. Instrum. Sci.* **2022**, JAIS–264 (2022).
167. Insero, G. et al. Measuring molecular frequencies in the 1–10 μm range at 11-digits accuracy. *Sci. Rep.* **7**, 12780 (2017).
168. Tominaga, T. & Kubo, N. Adaptive estimation of measurement noise to improve the performance of GNSS single point positioning in dense urban environment. *J. IPNT* **8**, 1–8 (2017).
169. Angrisano, A. et al. Adaptive estimation of measurement noise to improve the performance of GNSS single point positioning in dense urban environment. *Acta. Geod. Geophys.* **48**, 149–161 (2013).
170. Liddell, H. G. et al. *A Greek–English Lexicon* (Clarendon, 1996).

## Author contributions

H.K.M.T., C.B., A.B., O.C., G.C., A.G., M.H., I.L.R., G.L., Z.L. D.L.P., J. Marteau, L.O., S.S.V.S.R., S.S. and D.V. wrote the text. H.K.M.T., C.B., A.B., O.C., Z.L., J. Marteau, L.O. and K.S. prepared the figures. All authors reviewed the manuscript.

## Competing interests

The authors declare no competing interests.

## Additional information

**Peer review information** *Nature Reviews Methods Primers* thanks Stylianos Chatzidakis, Luigi Cimmino and the other, anonymous, reviewer(s) for their contribution to the peer review of this work.

**Publisher's note** Springer Nature remains neutral with regard to jurisdictional claims in published maps and institutional affiliations.

Springer Nature or its licensor (e.g. a society or other partner) holds exclusive rights to this article under a publishing agreement with the author(s) or other rightsholder(s); author self-archiving of the accepted manuscript version of this article is solely governed by the terms of such publishing agreement and applicable law.

## Related links

**AquaMuography Research Facility:** <https://aqualine.muographers.org>  
**Definition of radiography:** <https://dictionary.cambridge.org/dictionary/english/radiography>  
**Facility for High Timing Accuracy for Fundamental Physics Experiments of the Italian National Metrological Institute:** <https://fraternise.inrim.it/fraternise-english>  
**Introductory videos:** <https://www.youtube.com/@MUOGRAPHIX/videos>  
**MUODIM:** <https://muodim.com/>  
**MUOGRAPHIX:** <https://news.muographix-u-tokyo.ac.jp/>  
**News article about the hidden corridor:** <https://www.bbc.co.uk/news/world-middle-east-64825526>  
**Oven-controlled crystal oscillators:** <https://www.microtron.be/media/c78fa7db61fd72aec4c52d1a2ae40826/thunderbolt-ptp-grandmaster-clock-ptp-gm200.pdf>  
**Rubidium CSAC (SPARKX SPX 14830):** <https://www.sparkfun.com/products/14830>  
**US Department of Homeland Security PNT Program:** <https://www.dhs.gov/science-and-technology/pnt-program>  
**UTokyo–Wigner Joint Laboratory:** <https://muography-tpk.wigner.hu/newcut/>  
**White Rabbit:** <https://white-rabbit.web.cern.ch/>

© Springer Nature Limited 2023